Journal Pre-proof

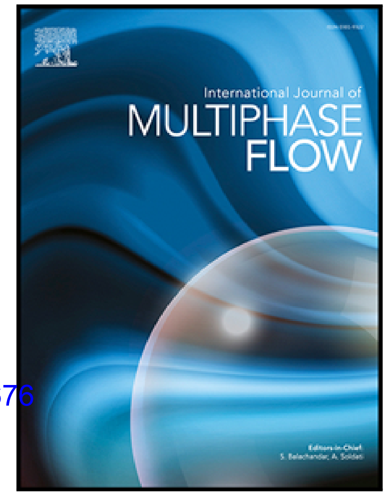

Accuracy of bed-load transport models in eddy-resolving simulations

Gianmarco D'Alessandro, Zvi Hantsis, Cristian Marchioli,
Ugo Piomelli

PII: S0301-9322(21)00124-5
DOI: https://doi.org/10.1016/j.ijmultiphaseflow.2021.103676
Reference: IJMF 103676

To appear in: *International Journal of Multiphase Flow*

Received date: 25 December 2020
Revised date: 18 April 2021
Accepted date: 23 April 2021

Please cite this article as: Gianmarco D'Alessandro, Zvi Hantsis, Cristian Marchioli, Ugo Piomelli, Accuracy of bed-load transport models in eddy-resolving simulations, *International Journal of Multiphase Flow* (2021), doi: https://doi.org/10.1016/j.ijmultiphaseflow.2021.103676

Graphical Abstract

Accuracy of bed-load transport models in eddy-resolving simulations

Gianmarco D'Alessandro, Zvi Hantsis, Cristian Marchioli, Ugo Piomelli

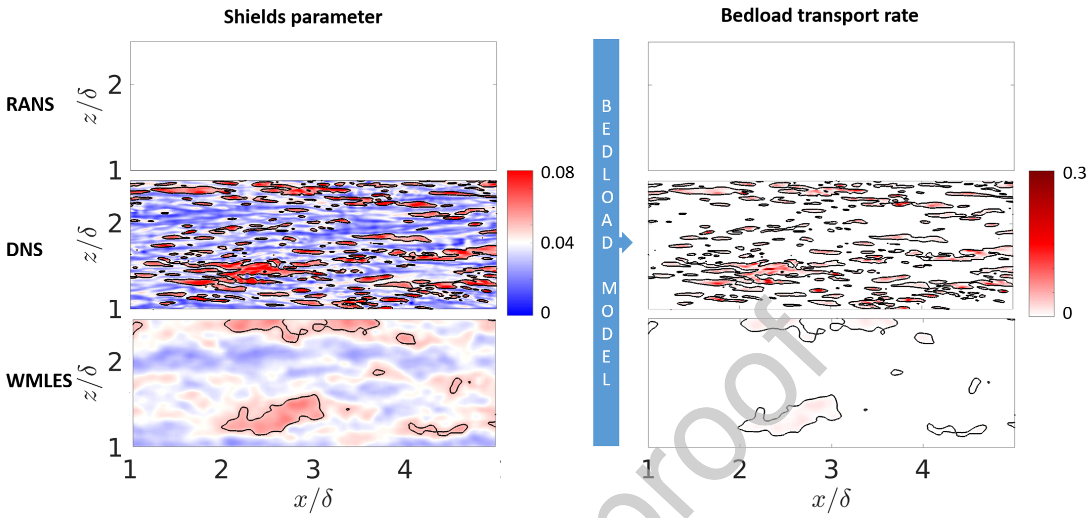

Highlights

Accuracy of bed-load transport models in eddy-resolving simulations

Gianmarco D'Alessandro, Zvi Hantsis, Cristian Marchioli, Ugo Piomelli

- The high resolution of the eddy-resolving Navier-Stokes solvers is incompatible with RANS-based bed-load transport models.
- The discrepancies are limited to subcritical values of the Shields parameter, where transport is governed by bed-load motion.
- The bed-load predictions of DNS-based models show qualitatively similar behaviour.
- Time averaging on a window of the order the large-eddy turnover time improves the predictions of bed-load transport models.
- The same behaviour is observed in turbulent channel flow over smooth and rough walls, and over a two-dimensional fixed dune.

Accuracy of bed-load transport models in eddy-resolving simulations

Gianmarco D'Alessandro[a,*] (Co-ordinator), Zvi Hantsis[a], Cristian Marchioli[b] and Ugo Piomelli[a] (Co-ordinator)

[a]Dept. of Mechanical and Materials Engineering, Queen's University, McLaughlin Hall, 130 Stuart Street, Kingston, Ontario, Canada K7L 3N6
[b]Dept. of Engineering and Architecture, University of Udine, Udine, ITALY

ARTICLE INFO

Keywords:
Bed-load transport
Open-channel flow
Dune
Turbulence
RANS Simulation
Large Eddy Simulation
Direct Numerical Simulation

ABSTRACT

This work investigates the accuracy of commonly used bed-load transport models when applied in combination with high-resolution Navier-Stokes solvers. Empirical bed-load models predict the transport rate of sediments based on the average bottom shear-stress, while eddy-resolving approaches allow for a space- and time-dependent description of the bottom shear-stress distribution. We discuss the effect that a fine-graining of the stress distribution provided by the flow solver has on the transport model prediction, and we examine the space and time scales at which the averaged values of the transport rate, obtained using the local stress distribution, converge to the transport rate predicted using the average stress. To this aim, we performed Direct Numerical Simulation of a channel flow and used the resulting database to mimic Wall-Resolved and Wall-Modelled Large-Eddy Simulations. We compared the prediction of several bed-load transport models to experimental measurements in order to identify and highlight the limitations that stem from the coupling of these models with eddy-resolving techniques. We find that for small values of the Shields parameter (ratio of viscous and gravitational forces) the fine spatial and temporal resolution of wall-resolved simulations can yield overestimation of the bed-load transport rate; whereas more coarse-grained methods, such as wall-modelled Large Eddy Simulation, result in improved predictions. We also show that a short-time averaging of the force exerted by the fluid on the sediments, which we tested in three different configurations (channel flow with smooth and rough walls and flow over an idealized two-dimensional river dune), improves the accuracy of the bed-load transport predictions, thus providing indications about the flow scales that control the transport process.

1. Introduction

Sediment-laden flows are of great practical importance, as they occur in a wide variety of natural and industrial processes, from soil erosion and sediment transport in streams and rivers, to materials handling (Nielsen, 1992). A detailed physical understanding and an accurate modelling of sediment transport dynamics is crucial to predict the effect that the resulting patterns, commonly termed bedforms, have on the overall bed morphology and sediment transport rates (Kidanemariam and Uhlmann, 2017). Sediment transport is mainly determined by the action of the flow, which removes sediment from the bed causing its erosion, by the effect of gravity, which drives sediment settling, and by the mixing induced by turbulence via the momentum exchange between the sediments and the carrier fluid. Turbulence, in particular, plays a crucial role in most natural flows, where the presence of coherent structures associated with significant vorticity, velocity and pressure fluctuations is known to affect the local bottom shear-stress, the entrainment process and consequently the bed morphology (Best, 2005; Livingstone et al., 2007; Papadopoulos et al., 2020).

In an effort to gain fundamental knowledge of the bed-form morphodynamic changes, a large number of investigations have been carried out in the past. Experiments have been extensively performed to examine aspects such as near-bed transport (van Rijn, 1984c; Nielsen, 1992; Niño and García, 1998; Cheng, 2002; Wong and Parker, 2006), deposition

*Corresponding author
ORCID(s):

or settling (Oliver, 1961; Batchelor, 1972; Davis, 1985), suspended transport (van Rijn, 1984a, 1987; Celik and Rodi, 1991; Garcia, 1991; Hay and Sheng, 1992), and bedform evolution (Best, 1996, 2005; Venditti et al., 2005; Parsons et al., 2005; Reesink and Bridge, 2007, 2009; Kocurek et al., 2010; Coleman and Nikora, 2011; Reesink et al., 2018; Unsworth et al., 2018).

In spite of the progress made, however, achieving a complete understanding of the mechanisms that drive the bed morphodynamics has been and still remains a challenging task from an experimental perspective. This is due to a number of factors, such as the need to consider idealized boundary conditions, the difficulty of detecting the early stages of pattern formation or the limited extent of the observation time window (Scherer et al., 2020), which all stem from the complex interaction between the sediment particles and the driving turbulent flow. Additionally, field measurements of the sediment flux during morphogenetic events are currently difficult, if not impossible, to obtain (Vittori et al., 2020).

A useful complementary tool to overcome these difficulties is represented by numerical simulations, which can be used to analyze the interactions between sediment particles and the carrying flow, especially in the near-bed region. In most of the previous numerical works, the background turbulent flow has been typically obtained by coupling a Reynolds-Averaged Navier-Stokes (RANS) equations solver, with a sediment continuity equation to describe the sediment-bed evolution (Paola and Voller, 2005). The hydrodynamic and morphodynamic problems are then linked by an algebraic expression for the bed-load transport rate, which will be indicated as Φ in its dimensionless form, hereinafter. These expressions allow to estimate Φ as a function of the sediment properties (specific gravity, grain size, etc.) and flow properties, notably the space- and/or time-averaged bed shear-stress, indicated as $\langle \tau_w \rangle$ hereinafter (the angle brackets denote time- and space-averaged quantities). Some attempts have been made to improve the predictive capability of these expressions by including the effect of turbulent burst phenomena (Cao, 1999; Lee et al., 2012; Salim and Pattiaratchi, 2020). In one such attempt, Guan et al. (2021) have shown that bed-load sediment transport is strongly influenced by the near-wall coherent structures and by the inertia of the particles travelling near the bed; concluding that the bed-load transport rate is not uniquely determined by the bottom-shear stress.

The bed-load transport models often depend on a threshold value of τ_w, referred to as the critical bed shear-stress $\tau_{w,cr}$. Above this thershold, sediment motion takes place. Many definitions of $\tau_{w,cr}$ are available in the literature (Debnath and Chaudhuri, 2010b), derived by measuring the amount of sediment eroded over a certain time span as a function of the average bed shear-stress (which, in most experiments, is evaluated from the extrapolation of the Reynolds shear-stresses). The specific definition adopted has a strong impact on the model calibration and, hence, on the prediction of the bed-load transport and suspended sediment transport. This is the most sensitive aspect, as far as simulation of the morphodynamics of alluvial and coastal environments is concerned. In the past, RANS-based models have been applied to the study of sediment transport over sand bedforms (Parsons et al., 2004; Lefebvre, 2019; Yamaguchi et al., 2019), highlighting the influence of the bedform geometrical properties on the mean flow characteristics: Parsons et al. (2004) focused on idealized two-dimensional transverse dunes, while Lefebvre (2019) and Yamaguchi et al. (2019) studied natural three-dimensional bedforms. More recently, Chiodi et al. (2014) and Ahadi et al. (2018) performed RANS of sediment transport in open-channel flow using a two-fluid model to relate the bed-load sediment transport to the mean flow quantities. This approach, however, fails to explain some of the hydrodynamics and morphodynamics mechanisms (Weaver and Wiggs, 2011; Wu et al., 2017).

The main issue with the empirical models just discussed is that the actual bed-load transport rate depends on the instantaneous spatial distribution of the bottom shear-stress, which represents the footprint of turbulence, and not on its space- or time-averaged value. An example of such distribution is provided in Figure 1, where a typical evolution (in time, labelled as t, or in space, along the horizontal flow directions, labelled as x and z) of the bottom shear-stress, $\tau_w(x, z, t)$, is shown. Although the time- and space-averaged bottom shear-stress, $\langle \tau_w \rangle$, is, in this example, smaller than the critical value, the instantaneous/local bottom shear-stress exceeds

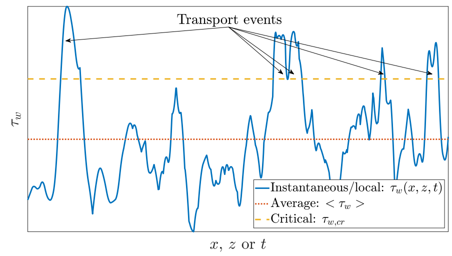

Figure 1: Typical evolution (in time or in space) of the instantaneous/local bottom shear-stress, $\tau_w(x, z, t)$. The dotted and dashed horizontal lines show the time- and space-averaged value $\langle \tau_w \rangle$, and the critical value $\tau_{w,cr}$ that is used by the empirical bed-load transport models.

the critical value in some instances. This generates instantaneous/local transport events that would not be captured by a model based on the average stress. Clearly, empirical models cannot incorporate all the complexities of the phenomenon (which include a wide range of temporal and spatial scales, threshold effects, non-linearities and dependence on flow conditions [Ancey 2020a]) and may lead to inaccurate estimations, especially when used outside their limit of applicability (Meiburg and Kneller, 2010), as we will also show in this paper.

An alternative approach is represented by Direct Numerical Simulation (DNS), which has benefited from the increased computational resources of modern computers, and has opened a new promising branch of research aimed at exploring the *micro-mechanics* of sediment transport, namely the physical processes occurring at the scale of sediment particles (Kidanemariam and Uhlmann, 2014, 2017; Biegert et al., 2017; Vowinckel et al., 2019b; Mazzuoli et al., 2020; Vittori et al., 2020; Akiki and Balachandar, 2020).

Within the DNS-based Euler-Lagrange framework, the sediment transport processes occurring at the mesoscale can be simulated by tracking a large number of particles that are assumed to be smaller than the grid size of the fluid solver and modelled as mass points that move under the action of the flow hydrodynamic forces. An overview of the most recent point-particle DNS studies is provided in Vowinckel (2021) and shows that these types of simulations are able to reproduce bed-form evolution of ripples and dunes in unidirectional and oscillatory flows, especially when particle-particle interactions of contact and collision are accounted for.

The microscale of individual particle-particle interactions, on the other hand, can be represented by particle-resolved simulations in which the motion of each particle is computed by resolving the flow field around it: this requires that the grid size be significantly smaller than the particle diameter. The increased spatial and temporal accuracy comes at the expense of a much higher computational cost, compared to the RANS-based approach, but allows the explicit calculation of the distributions of sediment concentration, shear stress and sediment flow rate. The availability of this kind of fully-resolved (in space and time) information is crucial to shed light not only on the effect of the flow on the bed evolution but also on the effect of the sediment patterns on the flow properties and, in turn, on the sediment transport mechanics (Vowinckel, 2021).

In this context, Kidanemariam and Uhlmann (2014) performed DNS simulation of flow over a bed of mobile, spherically-shaped particles. They accurately predicted the formation of dunes from a flat bed under the action of laminar and turbulent flow. Mazzuoli et al. (2020) examined the transport of sediments in a turbulent oscillating boundary layer over an initially flat bed of movable mono-sized spheres. They found that the dynamics of sediments that are suspended is strongly related to the properties of turbulence, which depend on the distance from the bed surface and on the phase of the wave cycle. Vittori et al. (2020) extended the study by Mazzuoli et al. (2020) to focus on the bed-load layer. They concluded that the empirical formulae present in literature to predict bed-load transport are accurate only in a specific range of application: above the condition of steady bed-load transport and below the condition of suspended sediment transport. In a series of papers (Vowinckel et al., 2017a,b; Papadopoulos et al., 2020), Frohlich and co-workers used DNS to investigate the momentum fluxes and hydrodynamic stresses within and above a mobile granular bed in a turbulent open-channel flow laden with mono-disperse spherical sediment particles (either partially mobilized or all in motion). The momentum fluxes were computed as temporal and spatial averages following a double-averaging methodology that allows the DNS data to be convoluted in a rigorous way, thus providing detailed description and quantification of the physical mechanisms involved in momentum exchanges. It was found that partially-mobilized particles create streamwise bedforms that cause spanwise heterogeneities and yield significant form-induced momentum fluxes. It was also shown that particles always take up a substantial amount of the momentum supplied, which ultimately increases the channel hydraulic resistance, enhancing and stabilizing secondary flows.

The main advantage of fully-resolved simulations is their capability to provide in a deterministic manner the critical amount of sediment flow rate that is required to trigger sediment resuspension from the bed, this information being essential for development of physics-based erosion and bedload transport models (Mazzuoli et al., 2020; Vittori et al., 2020). On the other hand, these simulations are very expensive from a computational point of view and can only be made affordable by reducing the number of sediment particles composing the bed or by limiting the flow Reynolds number to values well below a real physical application (Vowinckel et al., 2019a).

In principle, a further possibility to reduce the computational cost consists in modelling the erosion/entrainment process in a way similar to what is done in RANS-based approaches, i.e., using an Eulerian approach that solves a transport equation for the sediment mass (Vowinckel, 2021). This strategy was employed recently by Zgheib et al. (2018a,b), who applied DNS to the study of ripple formation from a flat bed at relatively low Reynolds number. The authors focused on the flow regime where the only mode of sediment migration is bed-load transport and did not solve the sediment-concentration transport equation. Rather, the morphodynamics equation, which involves a bed-load transport model, erosion and deposition, was considered. They observed various bed-form interactions during the formation process, such as lateral linking and merging, as well as evolution of ripples from a longitudinal to a transverse orientation. However, using the same empirical models developed for RANS in combination with DNS goes well beyond the applicability limits of the models. In addition, there are very few models that estimate (rather than compute explicitly) the bed-load transport rate based on the local bottom shear-stress distribution, *e.g.* Lee et al. (2012).

In this context, a crucial question that arises is related to the space and time resolution of the bottom shear-stress distribution that is required to yield satisfactory estimates of the bed-load sediment transport by a given model. This question is particularly relevant when eddy-resolving methods, like Large-Eddy Simulation (LES), are used. These methods represent an approach intermediate between RANS and DNS, in that they combine more affordable computational costs (compatible with practical applications) and reasonably-adequate predictive capabilities.

In LES, in particular, the flow dynamics is resolved at a much finer scale than RANS. The spatial resolution is designed and tuned to capture the turbulent structures that are expected to influence the flow dynamics the most, while only the small scales of the flow are modelled. Due to the lower discretization accuracy (compared to DNS) a full resolution of the flow around the particles is not possible in this type of simulations (Marchioli, 2017). Therefore, an Eulerian approach is taken to solve the sediment transport problem, where the sediment phase is modelled as a continuum. This approach has considerably lower computational demands than its Lagrangian counterpart. Because of its flexibility, LES has been widely used to study sediment transport in a variety of configurations and geometries. Zedler and Street (2001, 2006) simulated the transport of sediments over ripples under the action of steady or oscillatory flows, observing the role of Görtler vortices in the sediment entrainment mechanism. Chou and Fringer (2008) used LES to study the characteristic time scales of sediment transport in turbulent channel flow at high Reynolds number, and, in a successive work, to investigate the bed formation process for the case of sand ripples from a flat bed (Chou and Fringer, 2010). Khosronejad and Sotiropoulos (2014) implemented a hydromorphodynamic model to simulate the formation of sand waves in channel flow, which they later used to study the formation of Barchan dunes (Khosronejad and Sotiropoulos, 2017). In these studies the bed-load transport uses local and instantaneous bed shear-stress values in the models, despite the fact that these models were developed and calibrated with RANS solutions in mind, using average values only.

An important feature of LES, and of eddy-resolving methods in general, is that the computed bottom shear-stress fluctuates in space and time. Therefore, even if the average shear stress is below the critical value ($\langle \tau_w \rangle < \tau_{w,cr}$), the local values of the stress predicted by the flow solver can be above the threshold ($\tau_w(x,z,t) > \tau_{w,cr}$), the opposite being also possible when $\langle \tau_w \rangle > \tau_{w,cr}$. In other words, the average bed-load transport, $\langle \Phi(\theta) \rangle$, will differ from the bed-load transport based on averaged flow quantities, $\Phi(\langle \theta \rangle)$, with θ representing the Shields parameter. This hints to the possibility of applying successfully *local* models such as that of Lee et al. (2012), but poses issues too. One issue is related to the possibility of tuning the accuracy with which the bottom shear-stress distribution is provided by the flow solver to improve the estimate of the bed-load sediment transport by using the available empirical models. The other issue is related to the evaluation of the space and time scales at which $\langle \Phi(\theta) \rangle$ recovers $\Phi(\langle \theta \rangle)$. Both issues are associated to the type of LES that is performed: Wall-Resolved LES, referred to as WRLES hereinafter, resolves the wall layer, whereas Wall-Modelled LES, referred to as WMLES hereinafter, models it.

In WRLES, since the grid extends to the wall, the first grid point is in the linear region of the velocity profile, and the wall stress is evaluated using a finite differences approximation. With this approach, the fluctuations of τ_w are significant, their root-mean-square being approximately 37% of the mean value (Wu and Chou, 2003). In WMLES, on the other hand, the wall stress is calculated based on the velocity at the inner/outer layer interface point, usually located at $y = 0.05 - 0.1\delta$ (where δ is the water depth). An equilibrium stress layer is typically assumed, but other approaches are also possible (Piomelli, 2008; Larsson et al., 2016; Bose and Park, 2018). In this case, the fluctuations of τ_w are significantly lower than those of WRLES, since the velocity fluctuations at the interface are much smaller than those nearer to the wall. It is thus reasonable to expect that the predictive capability of a given sediment transport model will be different in WRMLES and in WMLES.

In this paper, we try to address these issues by performing a campaign of simulations characterized by different levels of spatial and temporal resolution, and also considering flow geometries that are relevant for sedimentation problems and are characterized by non-equilibrium flow conditions. Non-equilibrium conditions, which occur in the presence of separation, flow three-dimensionality, and/or strong acceleration for instance, are considered here to assess the performance of the selected transport models when these are used outside of their limit of applicability, namely equilibrium turbulence conditions, typical of plane channels, pipes or flat-plate boundary layers (Charru et al., 2013).

To this end, we will start by considering the DNS results for the case of plane channel flow, which will be used as reference as well as input for the various models. DNS data will be then filtered, *a posteriori*, to mimic typical WRLES, WMLES and RANS solutions; each solution approach will then be coupled with the selected transport models to compare the performance of the different combinations. This analysis will be repeated for a channel flow over rough walls, and for the case of flow over a model river-dune geometry, where flow separation, reattachment, adverse and favourable pressure-gradients occur (Balachandar et al., 2007; Stoesser et al., 2008; Omidyeganeh and Piomelli, 2011). The insights gained with this study will improve the understanding of the performances of morphodynamic models in eddy-resolving calculations, and their limitations.

In the following, the numerical methodology is introduced. Then, the bed-load transport models tested are reviewed, and the results of the present investigation are discussed. Finally, conclusions and recommendations for future work are given.

2. Methodology

In this section we summarize the features of the models considered in our study. First, the fluid flow solvers are presented. Then, the bed-load transport models are introduced.

2.1. Governing equations for the fluid phase

We study the dynamics of an incompressible Newtonian fluid, which is governed by the equations of conservation of mass and momentum:

$$\nabla \cdot \mathbf{u} = 0 \tag{1a}$$

$$\frac{\partial \mathbf{u}}{\partial t} + \nabla \cdot (\mathbf{u}\mathbf{u}) = -\nabla P + \frac{1}{Re_b}\nabla^2 \mathbf{u} \tag{1b}$$

where all quantities are made dimensionless using the bulk velocity, u_b, the half channel height δ, the fluid density ρ, and the kinematic viscosity ν; the Reynolds number is $Re_b = u_b\delta/\nu$. The instantaneous velocity vector is $\mathbf{u}$, with (u, v, w) the velocity components along the streamwise, wall-normal, and spanwise coordinate directions (x, y, z), respectively. Finally, P is the dimensionless pressure.

2.2. Numerical methods

The data used for the evaluation of bed-load transport models were obtained from DNS or LES of the flow in various geometries, which are described in detail in section 3.2. For the DNS calculations, Equations (1a) and (1b) are solved on a staggered Cartesian grid. All derivatives are calculated by second-order, centered finite difference approximations, and a fractional step method (Kim and Moin, 1985) is used. A third-order Runge-Kutta scheme is used for the time advancement of the convective and diffusive terms in the streamwise and spanwise directions, while the diffusive term in the wall-normal direction is discretized using the second-order implicit Crank-Nicolson scheme. Periodic boundary conditions are applied in the streamwise and spanwise directions and a no-slip condition is applied at the bottom and top walls. The code has been extensively validated for turbulent flows of this type (Keating et al., 2004; Scalo et al., 2012; Yuan and Piomelli, 2014; Wu et al., 2019).

For the LES calculations, the filtered NS equations are solved. A spatial filter, with width proportional to the grid size, is applied to the flow field: All scales smaller than the filter width are modelled. The filtered NS equations read as

$$\nabla \cdot \tilde{\mathbf{u}} = 0 \tag{2a}$$

$$\frac{\partial \tilde{\mathbf{u}}}{\partial t} + \nabla \cdot (\tilde{\mathbf{u}}\tilde{\mathbf{u}}) = -\nabla \tilde{P} + \frac{1}{Re_b}\nabla^2 \tilde{\mathbf{u}} - \nabla \cdot \tilde{\tau} \tag{2b}$$

where $\tilde{\cdot}$ represents filtered quantities and $\tilde{\tau} = \widetilde{\mathbf{u}\mathbf{u}} - \tilde{\mathbf{u}}\tilde{\mathbf{u}}$ is the sub-filter scale stress tensor, which is modelled using the dynamic eddy-viscosity model (Germano et al., 1991; Lilly, 1992) with Lagrangian averaging (Meneveau et al., 1996). These equations are solved on a curvilinear, non-staggered grid with a Finite Volume approach that is second-order accurate in space. The fractional step method (Kim and Moin, 1985) is used in this case as well. A second-order Adams-Bashforth scheme is used for the time advancement of the convective and diffusive terms in the streamwise and spanwise directions, while the diffusive term in the wall-normal direction is discretized using a second-order implicit Crank-Nicolson scheme. Periodic boundary conditions are applied in the streamwise and spanwise directions and a no-slip condition is applied at the bottom wall, while the top boundary is modelled as a fixed free surface:

$$\frac{\partial u}{\partial y} = \frac{\partial w}{\partial y} = 0 \text{ and } v = 0 \tag{3}$$

2.3. Bed-load transport models

The bed-load transport process is determined by the balance between the force exerted by the fluid on the particle and the resisting force resulting from gravity, friction (due to the contact with other particles), and cohesive forces. Cohesive forces are relevant when the bed is formed by clay or sand particles containing significant amounts of water; this type of particle-particle interaction is more prominent for smaller particles (Warren, 2013). There is, however, lack of understanding in cohesive-sediment erosion and suspension, and uncertainty in the methodologies and definitions used to estimate cohesive-sediment erosion thresholds. Therefore, in this study we neglect these forces and limit the source of uncertainty to the bed-load transport model (Debnath and Chaudhuri, 2010a; Vowinckel et al., 2019b). Also, we assume the bed to be formed of dry sand particles (quartz).

The uplifting force is related to the near-wall velocity which, in turbulent flows, exhibits random fluctuations. Moreover, in real configurations, the particles have different size and shape: This aspect, combined with the random behaviour of the flow, can make the particle erosion very hard to parametrize and predict (van Rijn, 1993). The ratio of the sand-grain size to the viscous sub-layer height is a sensitive parameter for sediment transport models (van Rijn, 1993), as it determines the fraction of particles that will be subjected to strong velocity fluctuations. This dimensionless parameter, the particle Reynolds number, is defined as $Re_p = d/\delta_\nu$, where $\delta_\nu = \nu/u_\tau$ is the viscous length scale, $u_\tau = (\tau_w/\rho)^{1/2}$ is the friction velocity, ρ is the fluid density, and d is the grain size. Shields (1936) determined the critical bottom shear-stress for initiation of motion as a function of the particle Reynolds number, and also measured the threshold shear-stress to initiate motion of particles of different size. This condition differs from that encountered by suspensions, which are characterized by prolonged motion of the particle in the water column (van Rijn, 1993; Niño et al., 2003).

Different definitions of the threshold bottom shear-stress can be found in the literature (Shields, 1936; van Rijn, 1984a; Niño et al., 2003). Many authors use a normalized grain diameter, defined as

$$d_* = d\left[\frac{(s-1)g}{\nu^2}\right]^{\frac{1}{3}} \tag{4}$$

where $s = \rho_s/\rho$ is the ratio between particle density ρ_s and fluid density ρ, and g is the acceleration of gravity, and they express the critical shear-stress as a function of this parameter (van Rijn, 1993).

The bottom shear-stress can also be normalized by the sediment specific gravity and sediment grain diameter to yield the "transport stage" or Shields parameter, θ:

$$\theta = \frac{|\tau_w|}{(s-1)\rho g d} = \frac{u_\tau^2}{(s-1)gd}. \tag{5}$$

All bed-load transport models considered are expressed in terms of either of these two non-dimensional parameters.

The non-dimensional bed-load transport is defined as:

$$\Phi = \frac{q_{bl}}{\sqrt{(s-1)gd^3}} \tag{6}$$

where q_{bl} is the volume of sediment transported as bed load per unit time and width. Most of the bed-load transport models commonly used in the literature assume that particle transport starts as soon as the Shields parameter exceeds the critical value:

$$\theta_{cr} = \frac{\tau_{w,cr}}{(s-1)\rho g d}. \tag{7}$$

We will consider the following models (in the figures, they will be referred to using the abbreviations provided below):

- EF76 (Engelund and Fredsoe, 1976):

$$\Phi = 18.74\theta(\sqrt{\theta} - 0.7\sqrt{\theta_{cr}}) \tag{8}$$

where $\theta_{cr} = 0.05$.

- FLvB76 (Fernandez Luque and van Beek, 1976):

$$\Phi = 5.7(\theta - \theta_{cr})^{1.5} \tag{9}$$

where θ_{cr} is determined from the Shields incipient motion curve (Shields, 1936), and is a function of the particle Reynolds number.

- P79 (Parker, 1979):

$$\Phi = 11.2\frac{(\theta - \theta_{cr})^{4.5}}{\theta^3} \tag{10}$$

where $\theta_{cr} = 0.03$.

- vR84 (van Rijn, 1984c):

$$\Phi = 0.053D_*^{-0.3}\left(\frac{\theta - \theta_{cr}}{\theta_{cr}}\right)^{2.1} \tag{11}$$

Here and in (12)-(13) below, θ_{cr} is determined from the re-adapted Shields diagram (van Rijn, 1993).

- N92 (Nielsen, 1992):

$$\Phi = 12\sqrt{\theta}(\theta - \theta_{cr}). \tag{12}$$

- NG98 (Niño and García, 1998):

$$\Phi = 42.9(\theta - \theta_{cr})(\sqrt{\theta} - 0.7\sqrt{\theta_{cr}}). \tag{13}$$

- C02 (Cheng, 2002):

$$\Phi = 13\theta^{1.5}\exp\left(-\frac{0.05}{\theta^{1.5}}\right) \tag{14}$$

with no dependency on a critical shear-stress.

- WP06 (Wong and Parker, 2006):

$$\Phi = 3.97(\theta - \theta_{cr})^{1.5} \tag{15}$$

where $\theta_{cr} = 0.0495$.

Some of these models (Engelund and Fredsoe, 1976; Parker, 1979; Cheng, 2002; Wong and Parker, 2006) are independent of the grain size (which means that either they assume a constant θ_{cr} or they exclude the existence of a threshold). The other models (Fernandez Luque and van Beek, 1976; van Rijn,

Table 1
Experimental datasets for bed-load transport considered in this study.

Model	d_*	θ
Paintal (1971)	63 – 562	0.01 – 0.07
Fernandez Luque and van Beek (1976)	22 – 83	0.04 – 0.08
Cheng (2002)	18 – 20	0.06 – 8.47
Wong and Parker (2006) (revisited the data of Meyer-Peter and Müller (1948))	80 – 729	0.06 – 0.29

1984b; Nielsen, 1992; Niño and García, 1998) depend on the grain size, and will be analyzed separately.

The model by Lee et al. (2012) was also implemented (indicated in the figures with the abbreviation L12). This model relies on a work-based criterion for particle motion and defines the bed-load transport instantaneously and locally based on the force exerted by the fluid on virtual sediment particles. The procedure used for this model differs from the empirical models in that the bed-load transport depends on the instantaneous flow velocity at a certain distance from the wall (equal to the radius of the sediment particles), rather than on the bottom shear-stress. The force acting on the sediment particles is then calculated using the instantaneous particle Reynolds number, Re_f, based on the instantaneous flow velocity, u_f, the particles diameter, d, and the kinematic viscosity, ν. Two conditions for transport are to be satisfied: the transport process begins when the force exceeds a threshold value for motion; at this point the particle starts moving on the channel bed but it is not re-entrained yet; actual erosion/transport takes place when the work done by the fluid force on the particle exceeds the work necessary to move the particle from its location.

3. Experimental and numerical data

The numerical datasets produced in this study have been compared to experimental datasets available in the literature. In the following we describe these datasets in detail.

3.1. Experimental datasets

The experimental datasets used for the validation of bed-load transport models are listed in Table 1, together with the range of parameters examined. The dimensionless sediment diameters range between 18 and 729, and, the Shields parameter ranges between 0.01 and 10.

Combining equations (4) and (5), and the definition of Re_p we obtain:

$$Re_p = \frac{u_\tau d}{\nu} = \sqrt{\frac{\theta}{d_*^3}} \tag{16}$$

which shows the relation between the particle Reynolds number, Re_p, the Shields parameter, θ, and the non-dimensional diameter, d_*. If we assume that Re_p is the main parameter characterizing the particle dynamics, then we can derive that:

- at low particle Reynolds numbers, when the viscous forces are significant, the Shields parameter, θ, and the non-dimensional diameter, d_*, are both relevant quantities to the physics of the problem;
- in highly turbulent flows, characterized by larger values of Re_p, the particles dynamics is mainly governed by the Shields parameter.

Notice that the dataset of Paintal (1971) focuses on very low values of θ but considers a wide range of values for d_*. The experimental dataset from Cheng (2002), on the other hand, focuses on larger values of θ, but a limited range of values for d_*.

Figure 2 gathers all the experimental data, and also shows a correlation of the data, obtained as a least-squares-regression power-law. Since the experimental data exhibit different power-law exponents in different ranges of θ, the least-square-regression was performed separately on five different intervals of $\langle\theta\rangle$. The expression of the piecewise power-law

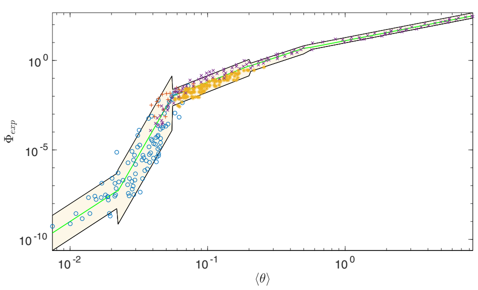

Figure 2: Experimental data from ○ Paintal (1971), + Fernandez Luque and van Beek (1976), ✳ Wong and Parker (2006), and × Cheng (2002); — best fit piecewise power law; ▭ 90% confidence range.

(PPL) so obtained is $\Phi = a\langle\theta\rangle^n$ where:

$$\begin{cases} a = 10, & n = 5 & \langle\theta\rangle < 0.022 \\ a = 6\times10^{14}, & n = 13.4 & 0.022 < \langle\theta\rangle < 0.055 \\ a = 63.74, & n = 3.022 & 0.055 < \langle\theta\rangle < 0.2 \\ a = 27.74, & n = 2.532 & 0.2 < \langle\theta\rangle < 0.5 \\ a = 12.66, & n = 1.496 & \langle\theta\rangle > 0.5 \end{cases} \tag{17}$$

We also plot the 90% confidence range, which was evaluated by discarding 5% of the points with the largest error above and below the PPL. The error is defined as

$$\epsilon_{PPL} = \frac{|\Phi_{exp} - \Phi_{PPL}|}{\Phi_{PPL}} \tag{18}$$

where Φ_{PPL} represents the value of the piecewise power law and Φ_{exp} refers the experimental measurements.

3.2. Numerical datasets

Three numerical datasets were used: two were obtained from DNS of plane channel flow with smooth and rough walls, the third from a WRLES of the flow over a 2D dune. The numerical results were manipulated to mimic WRLES, WMLES, and RANS using a procedure that will be described later, and coupled with the bed-load transport models presented in Section 2.3.

The DNS of channel flow with smooth walls was carried out at $Re_b = 21,400$ (based on the bulk velocity and the half-channel height) which corresponds to a friction Reynolds number $Re_\tau \simeq 1,000$, based on the friction velocity and the half-channel height. A computational domain of length (streamwise) $L = 6\delta$, width (spanwise) $W = 3/\delta$, and height (wall-normal) $H = 2\delta$ was discretized using $1024 \times 312 \times 512$ grid points in the streamwise, wall-normal, and spanwise directions, respectively. A uniform grid was used in the streamwise and spanwise directions, while a hyperbolic-tangent distribution was used in the wall-normal direction. This resulted in grid sizes $\Delta x^+ \simeq \Delta z^+ \simeq 6$, and $0.1 < \Delta y^+ < 39$, in wall units. The results agree very well with reference data, and are reported in detail by Hantsis and Piomelli (2020). A total of 160 instantaneous snapshots were collected, covering a time interval of $16t^*$, where $t^* = \delta/u_\tau$ is the large-eddy turn-over time, which represents the characteristic time of the large turbulent eddies.

The DNS of channel flow over rough walls was performed using the same code. The bulk-flow simulation parameters are similar to the smooth channel case. In particular, $Re_b = 21,400$, which corresponds to $Re_\tau \simeq 1,700$. A computational domain of length (streamwise) $L = 4\delta$, width (spanwise) $W = 2\delta$, and height (wall-normal) $H = 2\delta$ was discretized with $640 \times 530 \times 320$ grid points in the streamwise, wall-normal, and spanwise directions, respectively. It was shown (Hantsis and Piomelli, 2020) that the smaller domain has no effect on the flow in the region near the roughness. A uniform grid distribution was used in the streamwise and spanwise directions. In the wall-normal direction, a uniform grid covers the volume occupied by the roughness (128 grid points) and then a hyperbolic tangent distribution is applied up to the middle of the channel. This results in grid sizes $\Delta x^+ \simeq \Delta z^+ \simeq 11$, and $0.8 < \Delta y^+ < 48$, in wall units. Following the approach of Scotti (2006), the roughness is modelled by an Immersed-Boundary Method based on the Volume-Of-Fluid (VOF) approach. The roughness elements are randomly oriented ellipsoids with semi-axes k, $1.4k$, and $2k$, respectively, where k is 4% of the effective channel half-height. The resulting equivalent sand-grain roughness is $k_s \simeq 1.6k$. A total of 160 instantaneous snapshots were collected, covering a time interval equal to $22t^*$.

Finally, the LES of open channel flow over a 2D dune of height h was carried out at $Re_b = 18,900$ (based on the local bulk velocity and the water depth).

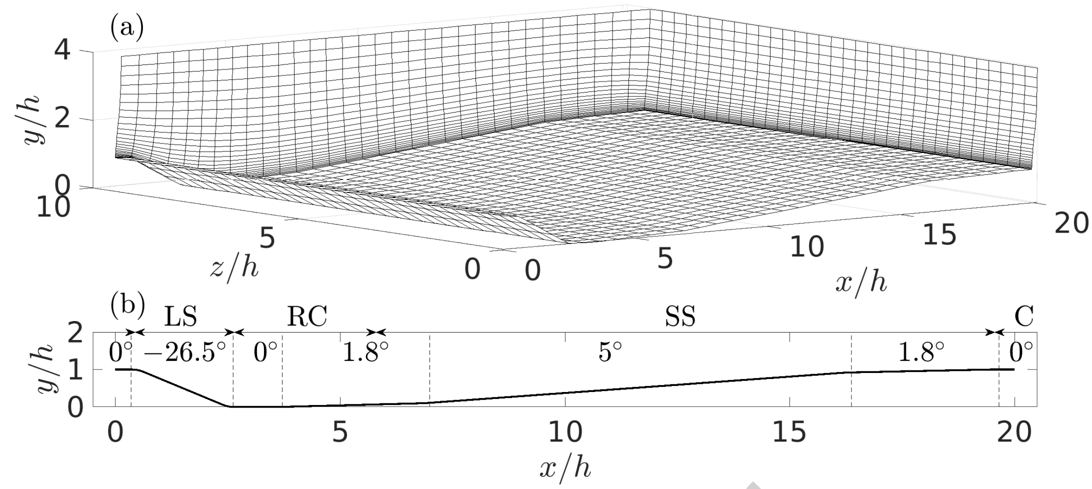

Figure 3: (a) Dune geometry and simulation mesh. Every eighth point of the mesh is shown for better visualization; (b) Dune bottom topology; the slope angle (in degrees) is shown in each region of the dune. LS: Lee Side; RC: Re-Circulation zone; SS: Stoss Side; C: Crest.

A computational domain of length (streamwise) $L = 20h$, width (spanwise) $W = 10h$, and water depth $\delta = 4h$ was discretized with $256 \times 98 \times 256$ grid points in streamwise, wall-normal, and spanwise directions respectively. We use the geometry studied by Balachandar et al. (2007), Stoesser et al. (2008) and Omidyeganeh and Piomelli (2011), shown in Figure 3 together with the computational grid. A uniform grid was used in the streamwise and spanwise directions, while a hyperbolic-tangent distribution was used in the wall-normal direction. This resulted in grid sizes $\Delta x^+ < 25$, $\Delta z^+ < 10$ and $0.1 < \Delta y^+ < 8$, in wall units. A large number (500) of instantaneous snapshots were collected, covering a time interval equal to $33t^*_{dune}$. The large-eddy turn-over time for the dune was evaluated at the section of the dune corresponding to the average water depth, $\overline{H}/h = 3.5$, as the ratio of average water depth to local friction velocity: $t^*_{dune} = \frac{\overline{H}}{u_\tau(H=\overline{H})} \simeq 60$. Large-eddy simulations of this problem, using the same numerical model and grid, were validated by Omidyeganeh and Piomelli (2011). Due to the dune geometry, the flow shows different characteristics: slow reversed flow over the lee side (LS), a strong re-circulation zone (RC) between $x/h = 2.5$ and $x/h = 6$, a re-attached boundary layer with increasing shear-stress over the upward slope, namely on the stoss side (SS), and finally a detached shear layer over the crest (C). Of course, such complexity of the flow field is reflected on the transport of sediment particles, with regions dominated by deposition of sediment grains onto the bed (LS and RC) and regions dominated by erosion (SS and C), as shown by Marchioli et al. (2006).

In such a complex bottom topography, the slope of the bed influences the transport rate also in terms of the threshold for transport. A negative angle (backward facing slope) decreases the critical shear-stress as the force exerted by the fluid on the particles and gravity act in the same direction, and vice-versa. The critical shear-stress is, therefore, modified to take into account the sloping bed as suggested by Lau and Engel (1999):

$$\frac{\theta_{cr,\alpha}}{\theta_{cr}} = \frac{\sin(\phi + \alpha)}{\sin(\phi)} \tag{19}$$

where α is the bed slope angle, and $\phi = \pi/6$ is the angle of repose of the bed, which represents the maximum slope that the sediment can withstand before collapsing under the action of gravity only. The variable $\theta_{cr,\alpha}$ is the critical shear-stress for the sloping bed, and θ_{cr} is the critical shear-stress for a horizontal bed.

In the DNS, the bottom shear-stress can be calculated directly from its definition, using finite differences. Then τ_w, which varies in x, z and time, is normalized and used as input to the bed-load transport models (8)-(15) to obtain $\Phi[\theta(x,z,t)]$. To mimic the WRLES, in which only the scales of motion larger than some characteristic length-scale (the filter width) are solved numerically, the DNS data were filtered explicitly with a spatial filter of width typical of wall-resolved calculations, i.e., 60 wall units in the streamwise direction, and 20 wall units in the spanwise direction. The velocity gradients (and hence the shear stress) were then calculated by means of finite differences and used to calculate $\Phi[\theta(x,z,t)]$ in all flow configurations.

For the WMLES, which typically uses coarser grids than WRLES, a spatial filter (with filter width 120 wall units) was applied to the streamwise velocity at an interface point located at $y_{IF}/\delta = 0.1$ (typical of the distance from the wall of the inner/outer layer interface [Balaras 2004; Kawai and Larsson 2012]). The bottom shear-stress is then evaluated assuming that the velocity satisfies the logarithmic law:

$$\frac{\widetilde{u}_{IF}}{u_\tau} = \frac{1}{\kappa}\log\left(\frac{y_{IF}u_\tau}{\nu}\right) + B - \Delta U^+ \qquad (20)$$

Here, $\widetilde{u}_{IF} = \widetilde{u}_{IF}(x,z,t)$ is the filtered velocity extrapolated at the inner-outer-layer interface, y_{IF}, $\kappa = 0.41$ is the von Kármán constant, and $B = 5$ is the logarithmic-law constant. Knowing $\widetilde{u}_{IF}$ and y_{IF}, a Newton-Raphson method is used to solve for u_τ from Eq. (20). The bottom shear-stress is then calculated as $\tau_w = \rho u_\tau^2 \cdot sign(\tau_w)$. No filtering was performed in the y direction because it would alter the mean velocity at the interface, which would not satisfy the logarithmic law any longer. The resulting wall stress returned by (20) would then be incorrect. To avoid this error, which would be artificially introduced by the filtering operation, and would not be present in an actual calculation, filtering was performed in the $xz-$plane only. The roughness function, ΔU^+, quantifies the increased drag due to the roughness. This function is equal to zero for the smooth wall, while the value measured in the DNS ($\Delta U^+ = 8.6$) was used in the rough-wall case. The resulting value of $\theta(x,z,t)$ was substituted into the models to obtain again $\Phi[\theta(x,z,t)]$. The application of this method to channel flows is straightforward, as such method was designed for wall bounded flows with a well defined and stable equilibrium layer between production and dissipation of turbulent kinetic energy, *i.e.* the logarithmic layer. However, in the flow over two-dimensional dune the equilibrium layer is disrupted by the detached shear layer over the dune crest and by the recirculation region, so that it is present only over the stoss side, when the favorable pressure gradient is weak (Spalart, 1986; Omidyeganeh and Piomelli, 2011). Therefore, the accuracy of the model in such regions is bound to be compromised.

RANS velocity fields, and specifically the average bottom shear-stress, were obtained from the DNS simulation by applying a spatial (in the xz-plane) and temporal average. The time- and space-averaged bed shear-stress $\langle\tau_w\rangle$ was then fed to the models (8)-(15), to yield a unique mean value of $\Phi(\langle\theta\rangle)$ (i.e., not dependent on position and time). For the dune calculation, the WRLES fields were treated as described above to yield WMLES and RANS bed-load predictions. Note that this approach separates the errors due to the modelling of the bed-load transport models from those due to uncertainties in the calculation of τ_w. In actual LES or RANS, the prediction of τ_w would be affected by numerical errors, and by the accuracy of the sub-filter scale or turbulence model. Only numerical errors are present in the DNS data, and those can be estimated by performing a grid refinement.

The main difference between the RANS approach and the eddy-resolving techniques lies in the fact that in RANS simulations the single value of $\langle\theta\rangle$ is used, and the resulting $\Phi(\langle\theta\rangle)$ is analogous to what would be measured in an experiment. In the eddy-resolving methods (DNS, WRLES and WMLES), the models must be applied locally and instantaneously, to compute $\Phi[\theta(x,z,t)]$. To make a meaningful comparison with the experiments, its plane- and time-averaged value, $\langle\Phi(\theta)\rangle = \langle\Phi[\theta(x,z,t)]\rangle$ must be used. The difference between $\Phi(\langle\theta\rangle)$ and $\langle\Phi(\theta)\rangle$ is then expected to be the cause of errors in the bed-load transport models.

This is illustrated in Figure 4. Panels a-d show contours of the local and instantaneous value of $\theta(x,z)$ obtained with the various techniques. We use, for this example, $\langle\theta\rangle = 0.04$ and $\theta_{cr} = 0.05$; the latter is a commonly used threshold value, while the former is chosen to illustrate the differences among the solution methods when $\langle\theta\rangle$ is close to θ_{cr}. For the RANS calculations (panel a), the Shields parameter is uniform, and equal to its average value,

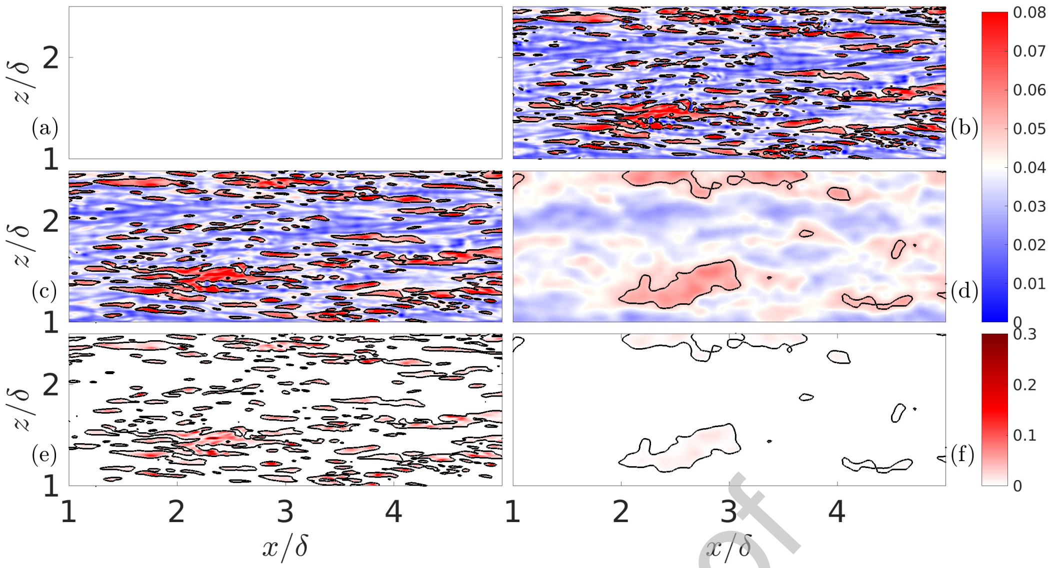

Figure 4: (a-d) Contours of the instantaneous Shields parameter $\theta(x, z)$, for a case with $\langle\theta\rangle = 0.04$. (a) RANS; (b) DNS; (c) WRLES; (d) WMLES. The value $\theta_{cr} = 0.05$ used in the model EF76 is shown as a solid contour. (e-f) Contours of the bed-load transport model $\Phi\,[\theta(x, z)]$ given by (8) with (e) WRLES; (f) WMLES.

$\theta(x, z) = \langle\theta\rangle$. The DNS (panel b) and WRLES (panel c) results show significant fluctuations of τ_w that result in regions where $\theta(x, z) \gg \langle\theta\rangle$. In the WMLES case (panel d) the solution is considerably coarser-grained than in the DNS and WRLES cases, and the regions where $\theta(x, z) \gg \langle\theta\rangle$ are less frequent and less intense.

Consider now, as an example, the model by Engelund and Fredsoe (1976), introduced in section 2.3, as reference. Since $\theta_{cr} = 0.05 > \langle\theta\rangle$, the model predicts no sediment lift-up. However, the eddy-resolving methods have regions where $\theta(x, z) > \theta_{cr}$ (the red regions). In these regions, the model predicts particle transport. This phenomenon was also analyzed by Vowinckel et al. (2016), who performed Lagrangian Particle Tracking in a channel flow at sub-critical Shields parameter and observed local occurrences of particle bed-load transport related to the local turbulent flow structures. The time scale of these events was of the order of the flow-through time and therefore not included in the mean flow characteristics. As a consequence of these local and short-lived events, the instantaneous transport model would yield localized regions of transport (Figures 4e and 4f), which would produce higher values of $\langle\Phi(\theta)\rangle$. This would be significant in the WRLES and DNS cases, less so in the WMLES, since the coarse-graining of the solution attenuates the fluctuations of the bottom shear-stress. All the models introduced in Section 2.3 exhibit the same behavior. This effect becomes more pronounced when $\langle\theta\rangle$ is close to θ_{cr}. If $\langle\theta\rangle > \theta_{cr}$ the fluctuating transport-stage may go below the threshold while the average is above it, so that regions of the flow are excluded from the calculation of the sediment transport rate.

The difference among DNS, WRLES and, to a larger extent, WMLES is in the spatial and temporal scale of the fluctuations of τ_w. With the grid used here for the WRLES, the solution in the viscous region of the wall layer is very well resolved, so that the difference between WRLES and DNS is hardly visible with the level of contouring used in figure 4. In WMLES, however, the grid is significantly coarser (so that only larger structures are resolved) and the bottom shear-stress is calculated using information obtained from the logarithmic layer. Therefore, the resulting τ_w will be smoother (i.e., less fluctuating) than in DNS. It must be pointed out that discriminating between the different types of near-wall flow structures is not necessarily relevant to the objective of this work. What matters is the ability of eddy-resolving methods to capture the effect of the turbulent structures on the wall shear-stress distribution. We do not aim at quantifying the discrepancy among bed-load transport predictions that result from the action of specific structures but, rather, we call the attention to the compatibility of bed-load transport models and eddy-resolving techniques.

The presence of sediment grains on the channel bed alters the geometry of the bed. Depending on their size and shape, the sediment particles can be described as roughness elements when $d << \delta$, or obstacles when $d \simeq \delta$ (van Rijn, 1984c). Wall roughness changes the flow dynamics in the near wall region, resulting in an increase of drag and more isotropic turbulent eddies. The sediment-grain diameter determines the roughness height k (a common value in sediment-laden flows is $k = 2d$) and different regimes can be identified based on the ratio of roughness height to the viscous length scale, δ_v: hydraulically smooth if $k/\delta_v < 4$, transitional if $4 < k/\delta_v < 80$, and fully rough if $k/\delta_v > 80$ (Jiménez, 2004). Since roughness increases the drag and alters the characteristics of the turbulence (in particular, decreasing the anisotropy of the Reynolds stresses) it will also change the spatial and temporal distribution of the Shields parameter, and hence of $\Phi\,[\theta(x,z,t)]$. To estimate the extent of this effect, we examined the results of a plane channel flow simulation over a rough wall with relative roughness $k = 0.04\delta$ (at the lower end of the fully rough regime). The same procedure as in the smooth case was used; the only difference is the fact that, the wall stress for the DNS was calculated by integrating the local and instantaneous VOF force. Since roughness may lead to flow separation behind the roughness elements, a pressure unbalance between the front and the rear of the elements is generated. The VOF force represents the total force exerted by the body on the fluid locally and includes both the pressure-induced form drag and the friction drag. For the WMLES the logarithmic law of the wall was modified by adding the roughness function ($\Delta U^+ = 8.6$), as previously discussed. The WRLES, WMLES, and RANS approaches were mimicked using the methodology previously described.

4. Results

We now compare the bed-load transport predictions obtained with the different approaches (DNS, WRLES, WMLES, and RANS) for smooth and rough walls. The bottom shear-stress distribution depends only on the approach and on the geometry. By varying the sediment characteristics, *i.e.* grain diameter and density, we can then span the range of $\langle\theta\rangle$ covered by the experiments, which fall into the "gravitational settling" regime defined by Finn and Li (2016), based on the scaling relations determined by Balachandar (2009). In this regime, the particle dynamics is mainly affected by settling, and the fraction of sediment carried as bed load, at a given $\langle\theta\rangle$, increases as d_* increases.

4.1. Smooth channel

First, we consider the bed-load transport models that are independent of d_* (Engelund and Fredsoe, 1976; Parker, 1979; Cheng, 2002; Wong and Parker, 2006), which are compared in Figure 5. For values of the Shields parameter well above the threshold ($\langle\theta\rangle > 0.1$), the curves generally collapse, independently of the computational approach. The model by Wong and Parker (2006) is consistently low, but all the other model predictions are within the scatter of the data. For small values of the Shields parameter, on the other hand, the results depend significantly on the computational approach used. These trends can be explained by the fact that, for low $\langle\theta\rangle$, the shear-stress distribution in DNS and WMLES is characterized by regions where $\theta(x,z,t)$ exceeds the threshold even if the mean Shields parameter is below the threshold, and vice-versa when $\theta(x,z,t)$ is slightly above it. For high $\langle\theta\rangle$, only the model non-linearity causes a difference among the various computational approaches, and this difference decreases as $\langle\theta\rangle$ increases. A similar behaviour was observed by Mazzuoli et al. (2020) in oscillatory flows, where the instantaneous bed-load transport rate is dependent on the flow characteristics as well as on the bottom shear-stress.

As expected, the RANS approach is in very good agreement with the experimental data for values of $\langle\theta\rangle$ larger than the critical value: the model constants are calibrated on average experimental data, so feeding an average bottom shear-stress to each model must, by construction, agree with the experiment. If the RANS approach is used, none of the

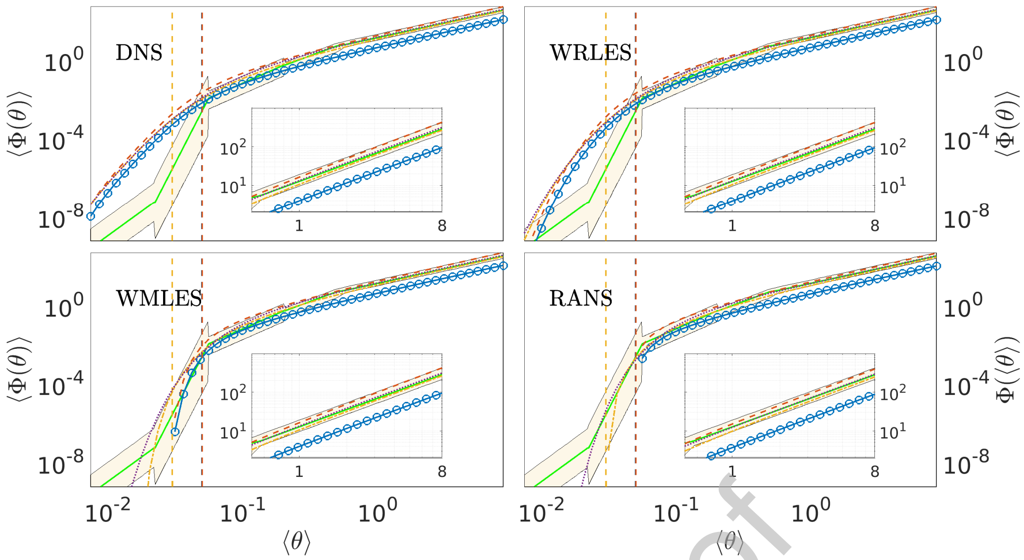

Figure 5: Comparison of the bed-load transport models independent of d_*. Piecewise power law; 90% confidence range; WP06; EF76; P79; C02; the vertical dashed lines represent the critical Shields parameter for each model (color-coded as indicated above). The inset figure is a zoom on the higher transport-stage range: $\langle\theta\rangle \in [0.5\ 8]$.

models will predict any transport when $\langle\theta\rangle < \theta_{cr}$; experimental measurements, however, show that some bed-load transport, albeit limited, actually takes place. An exception to this behaviour is the model by Cheng (2002), which is independent of a threshold Shields parameter, and, therefore, predicts accurately bed-load transport rates for $\langle\theta\rangle < 0.022$.

When the instantaneous bottom shear-stress calculated from the DNS or WRLES is used, on the other hand, the models consistently overpredict $\langle\Phi(\theta)\rangle$ when $\langle\theta\rangle$ is close or below the critical value, as discussed earlier. When $\langle\theta\rangle$ is well above the critical value, all the models predict accurately the bed-load transport rate, with the exception of the model by Wong and Parker (2006), which underestimates it roughly by a factor of 3. A possible cause of this discrepancy will be discussed later.

Overall, the model by Cheng (2002) is the one that provides predictions that fall most often within the confidence range. The model by Parker (1979) has a lower threshold and is, therefore, more accurate at lower values of the Shields parameter when combined with a RANS approach. When the model is combined with WMLES and WRLES, it predicts larger bed-load transport at low $\langle\theta\rangle$. For small values of the Shields parameter, in particular, WMLES provides more accurate results than WRLES (which overestimates the bed load) and RANS (which predicts no transport).

All the models perform poorly for very small values of the Shields parameter ($\langle\theta\rangle < 0.022$). However, in this range $\langle\Phi(\theta)\rangle$ is very small, $O(10^{-8})$, and these errors may have minor consequences. For $0.022 < \langle\theta\rangle < 0.055$ the comparison must take account of the large scatter in the available experimental data, which highlights the difference between DNS, WRLES, WMLES, and RANS: all models show the same trend, with DNS and WRLES predicting greater bed-load transport rate, WMLES being closer to the experimental data, and RANS predicting no bed-load transport. Above $\langle\theta\rangle = 0.055$ almost all curves fall well inside the confidence range, with the exception of the curve obtained using the model by Wong and Parker (2006). The reason for the poor performance of this model at large $\langle\theta\rangle$, is the fact that the relation for Φ (Equation 15) was calibrated against the data by Meyer-Peter and Müller (1948), by including a suitable correction (yellow

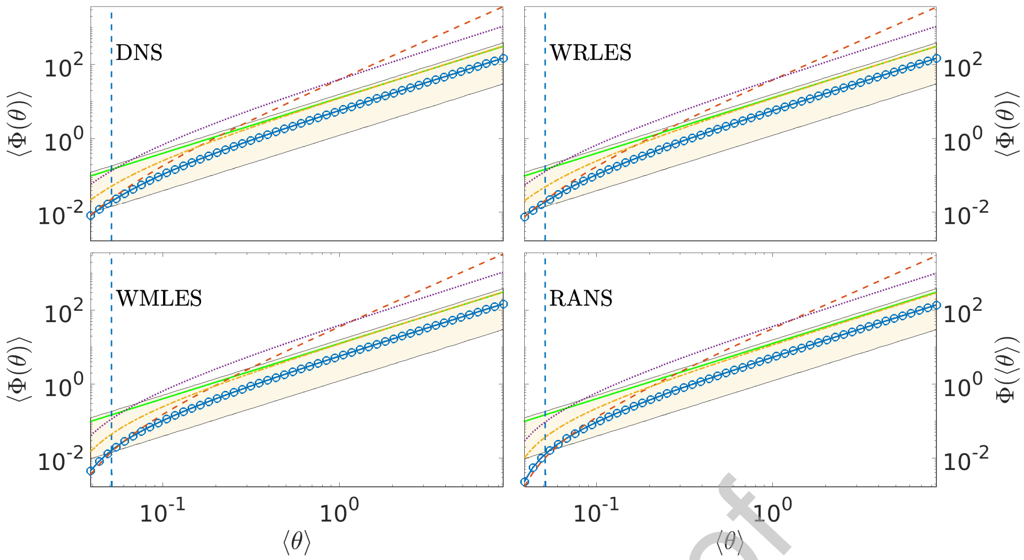

Figure 6: Comparison of the bed-load transport models, estimated for $d_* = 20$. Piecewise power law; 90% confidence range; FLvB76; vR84; N92; NG98. The vertical dashed lines represent the critical Shields parameter for each model (color-coded as indicated above).

markers in Figure 2). These experimental data lie exclusively in the range $0.055 < \langle\theta\rangle < 0.2$, and, therefore, the model fails to predict the bed-load transport outside of this range.

Next, we consider the transport models dependent on d_*. This dependency affects the models only in the definition of the threshold Shields parameter, θ_{cr}. Only two reference cases ($d_* = 20$ and 560) will be discussed. Figure 6 shows that, for small particle size ($d_* = 20$, $0.055 < \langle\theta\rangle < 10$), the difference between the four approaches is minimal, as expected given that $\langle\theta\rangle > \theta_{cr}$.

For large particle sizes ($d_* = 560$, $0.02 < \langle\theta\rangle < 0.055$), on the other hand, differences between the three approaches are apparent, as shown in Figure 7. For values of $\langle\theta\rangle$ below the critical value, the RANS-based transport prediction is, of course, $\Phi(\langle\theta\rangle) = 0$; the DNS results show values of $\langle\Phi(\theta)\rangle$ considerably larger than the experimental measurements, while both the WRLES and WMLES approaches yield bed-load transport values within the confidence range of the experimental measurements.

An important result of our analysis is shown in Figure 8, where the bed-load predictions obtained using the work-based model by Lee et al. (2012) are reported. A sediment grain size $d = 15\delta_v$ was assumed, therefore the velocity was extracted at $y = 7.5\delta_v$. These predictions are compared to those of the empirical models introduced in section 2.3. As expected, the model work-based behaves extremely well in the DNS case for a wide range of $\langle\theta\rangle$: the high spatial and temporal resolution is the numerical setup the model was designed for. On the other hand, when the velocity field is filtered in space (WRLES and WMLES) the local description of the flow is not fine enough to capture the microscopic effect of the fluid force on the particles, resulting in fewer occurrences of bed-load transport events: the peaks of the fluid force are smoothed and the work done by the particles is not calculated as accurately. The model performance is significantly affected by the simulated space and time scales, as these determine the shear-stress distribution that is fed into the model. A straightforward application of the work-based model to filtered flow fields does not seem to grant an accurate prediction, and hints to the necessity of recovering the effect of the filtered scales (e.g. through suitable sub-grid scale closures for the fluid velocity fluctuations) in order to improve results. The transport rates predicted us-

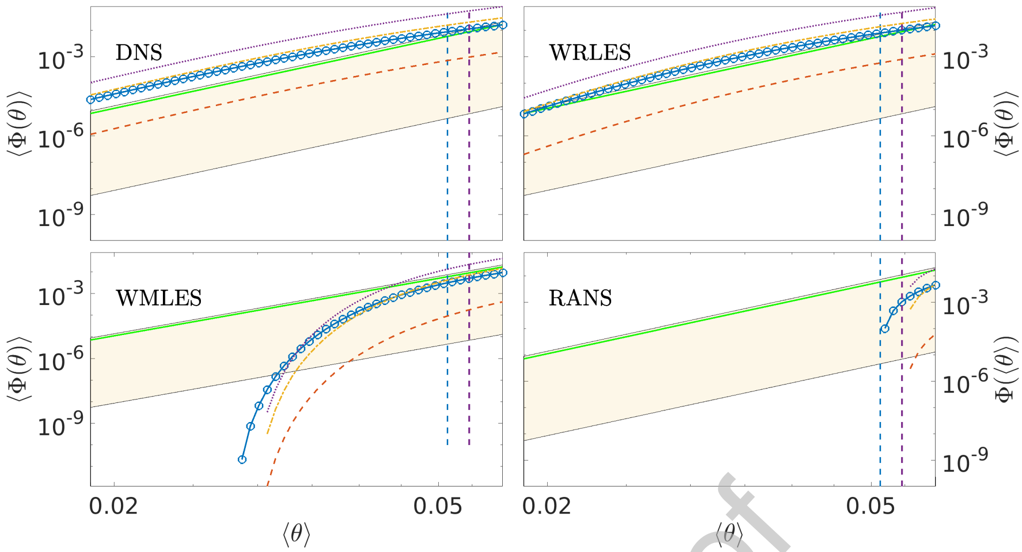

Figure 7: Comparison of the bed-load transport models, estimated for $d_* = 560$. Piecewise power law; 90% confidence range; FLvB76; vR84; N92; NG98; the vertical dashed lines represent the critical Shields parameter for each model (color-coded as indicated above).

ing the RANS approach are also shown. In this case, however, only the average fluid force can be used, and therefore the condition on the work done by the fluid force is omitted, neglecting the main physical mechanism on which this model is based.

4.2. Rough channel

The complex geometry of the sandpaper roughness disrupts the usual turbulence-generation cycle (MacDonald et al., 2019). As a consequence, the near-wall velocity fluctuations and the shear-stress fluctuations are higher compared with the smooth-wall case (the root-mean-square fluctuation of τ_w is almost three times larger). It is thus reasonable to expect a strong impact on the predicted bed-load transport.

Figure 9 shows the predictions of the bed-load transport models obtained using the data from the rough wall simulations: the DNS and WRLES approaches yield values of the bed-load transport larger than in the smooth case. This is due to the above-mentioned wider range of fluctuations of the bed shear-stress. The difference is clear for large values of the Shields parameter, where DNS and WRLES predict a bed-load transport roughly one order of magnitude larger than WMLES and RANS. Both the non-linearity of the models and the larger fluctuations of the rough wall flow field contribute to increase the differences among the various models. It must be noticed that the WMLES results do not vary significantly between the smooth case and the rough case. This happens because the near-wall region is not resolved in the WMLES approach: the bottom shear-stress is evaluated from the velocity extracted from the outer layer, which is unaffected by the presence of the roughness (MacDonald et al., 2019). The same qualitative behaviour is observed for the models dependent on the non-dimensional diameter d_*.

4.3. Short-time averaging

The results discussed in the previous sections indicate that the discrepancies observed in the wall-resolved calculations are due to the spatial and temporal variation of τ_w. Therefore, removing the fluctuations associated with these variations should improve the model accuracy (Guan et al., 2021). To further verify this assertion, we performed a short-time averaging of the local bottom shear-stress. This is done here as follows:

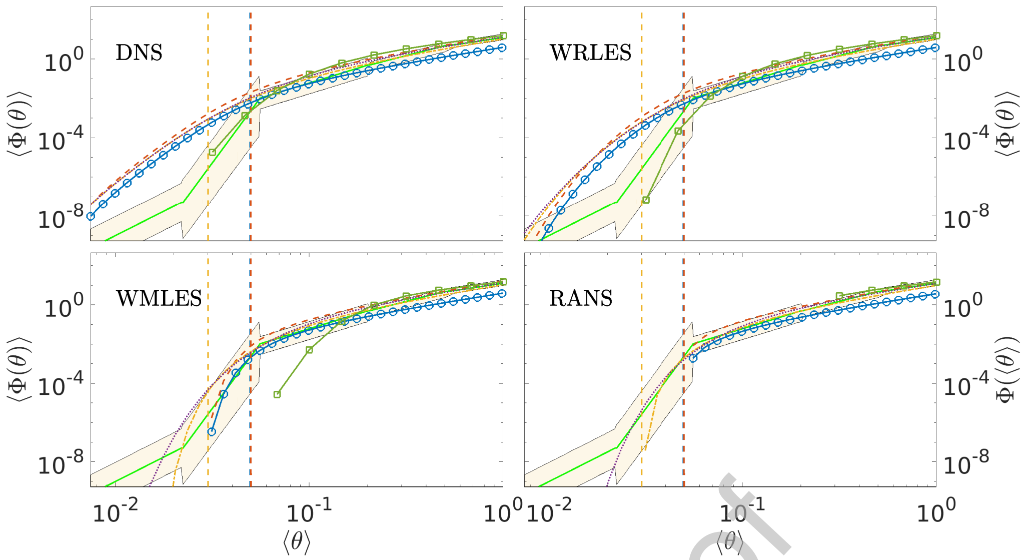

Figure 8: Comparison of WP06, EF76, P79, C02, and L12; the vertical dashed lines represent the critical Shields parameter for each model (color-coded as indicated above); Piecewise power law; 90% confidence range.

- first we calculate the moving average of the bottom shear-stress over a short time window, ΔT:

$$\overline{\tau_w}\,|_{\Delta T}\,(x,z,t) = \int_t^{t+\Delta T} \tau_w(x,z,\tilde{t})d\tilde{t} \quad (21)$$

- the local averaged Shields parameter is calculated: $\overline{\theta}\,|_{\Delta T}\,(x,z,t) = \frac{|\overline{\tau_w}|_{\Delta T}(x,z,t)|}{(s-1)\rho g d}$
- the bed-load transport rate is calculated from equations (8)-(15), $\Phi(\overline{\theta}\,|_{\Delta T})$.

The averaging should be performed over an interval long enough to decrease $\tau_{w,rms}$ but short enough to account for macroscopic changes of the flow dynamics (due to the presence of coherent structures, for instance). One would expect this interval to be proportional to the large-eddy turnover time (δ/u_τ). An "optimal" time-averaging window ΔT_{opt} can be chosen by requiring the model prediction to match the piecewise power-law given by Eq. (17). This time window, however, depends both on the value of $\langle\theta\rangle$ and on the specific model considered, being longer for strongly nonlinear models such as those by Parker (1979) and Cheng (2002). However, it would be impractical to change the averaging window depending on the value of $\langle\theta\rangle$, so we chose *a priori* three averaging windows (ΔT =1.5, 5, 10 δ/u_τ) and we compared the WRLES results to the experiments. Note that, since the filter-width used to obtain the WRLES quantities is very small, similar results would be obtained if the local velocity and wall stress were filtered in time only.

Figure 10 shows the time- and space-averaged bed-load transport, $\left\langle \Phi\left(\overline{\theta}\,|_{\Delta T}\right)\right\rangle$ predicted by each model, for varying averaging windows. The figure focuses on the range of Shields parameter close to the critical value, where the differences among the three averaging windows are most significant. All models show that a window $\Delta T = 1.5\delta/u_\tau$ is sufficient to lower the bed-load transport prediction so that it falls inside the confidence range. The purpose of the short-time averaging is to remove the small-scale fluctuations that cause the incorrect predictions of the RANS-based models. At the same time, it would be desirable to allow the model to respond to larger-scale unsteadiness (due, for instance, to the boundary conditions). From this perspective, the lowest value of ΔT for which the results become insensitive to the window size can be consid-

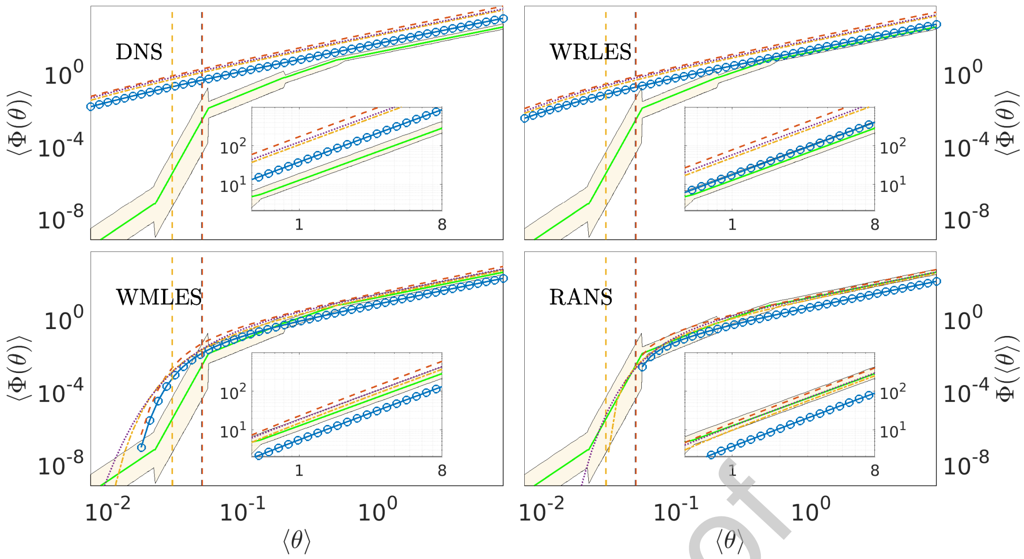

Figure 9: Rough channel case. Comparison of the bed-load transport models independent of d_*. Piecewise power law; 90% confidence range; WP06; EF76; P79; C02; the vertical dashed lines represent the critical Shields parameter for each model (color-coded as indicated above). The inset figure is a zoom on the higher Shields parameter range: $\langle\theta\rangle \in [0.5\ 8]$.

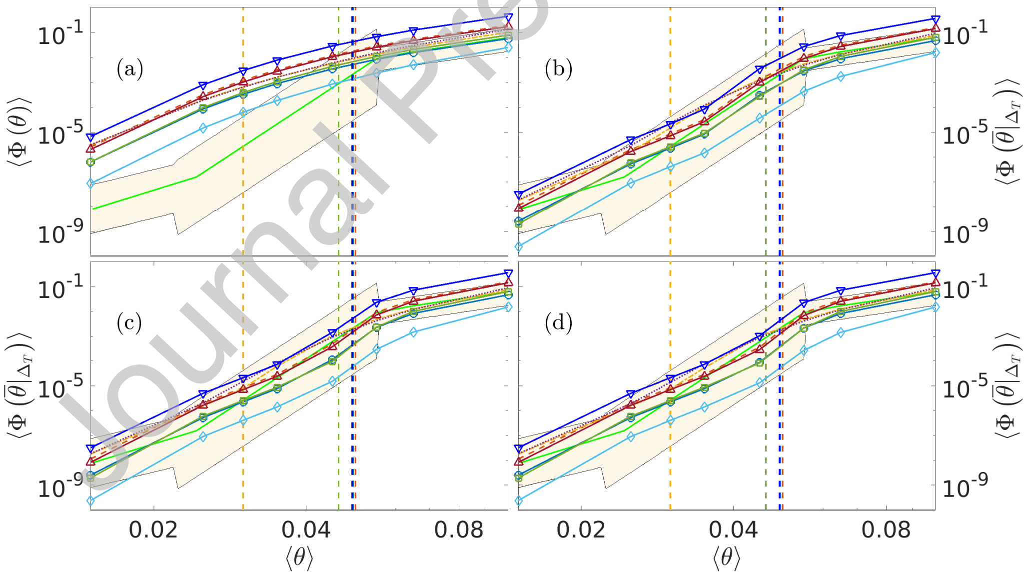

Figure 10: Comparison of the bed-load transport models with different size averaging windows. Piecewise power law; 90% confidence range; WP06; EF76; P79; C02 FLvB76; vR84; N92; NG98; the vertical dashed lines represent the critical Shields parameter for each model (color-coded as indicated above). (a) No averaging; θ averaged over (b) $\Delta T = 1.5\delta/u_\tau$; (c) $\Delta T = 5\delta/u_\tau$; (d) $\Delta T = 10\delta/u_\tau$.

ered optimal. For the cases examined in Fig. 10, $\Delta T = 1.5\delta/u_\tau$ appears to be the best choice.

Figure 10 shows that time-averaging improves the performance of the bed-load transport models for values of the Shields parameter lower than the critical value. For values well above the threshold, the averaging does not yield a considerable improvement of the transport rate prediction since $\overline{\theta}\,|_{\Delta T}\,(x, z, t)$ is always larger than the critical value. The same analysis performed on the bed-load transport models when DNS was used, shows that the ΔT_{opt} is up to two times larger than for WRLES. Much longer averaging intervals are probably needed in rough-wall cases to smooth out the much larger bottom shear-stress fluctuations.

4.4. Two-dimensional dune

In this section we analyze the performance of the transport models in the two-dimensional dune described in section 3.2. This geometry represents a simplified version of an alluvial dune and therefore values of d_* typical of alluvial streams were chosen. The size of river sand ranges from 60 µm to 2 mm and has a typical density of $\rho_s = 2650\,\mathrm{kg\,m^{-3}}$. Assuming $\rho = 1000\,\mathrm{kg\,m^{-3}}$, and $\nu = 1\times10^{-6}\,\mathrm{m^2\,s^{-1}}$ yields $d_* = 1.5{-}50$. The sediment-to-fluid-density ratio and grain diameter were chosen to obtain an average Shields parameter $\langle\theta\rangle \sim \mathcal{O}(0.1)$, for which the influence of the flow-solving methodology is more evident. Note that for this case no experimental reference data are available; thus, we highlight the regions where significant differences occur among the numerical techniques (WRLES, WMLES and RANS solutions), in order to identify the flow phenomena that require attention.

Figure 11 shows the streamwise distribution of the time- and spanwise-averaged Shields parameter, $\langle\theta\rangle_{zt}(x)$. After applying a time average over the entire simulation window, the bottom shear-stress estimated using WRLES, Time-averaged WRLES, and RANS is the same, albeit characterized by different local and instantaneous distributions. The Shields parameter distribution in the WMLES case, on the other hand, is noticeably different due to the inability of the wall-model to capture the non-equilibrium behaviour of the flow, especially in the recirculation regions and near reattachment (a mild, pressure-gradient-driven separation would also be problematic). The shear stress (and hence the Shields parameter) varies

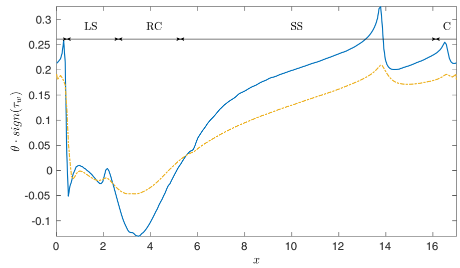

Figure 11: Streamwise distribution of the time and spanwise averaged Shields parameter, $\langle\theta\rangle_{zt}(x)$, over the two-dimensional dune, multiplied by the sign of $\langle\tau_w\rangle_{zt}(x)$ for better understanding of the flow regions. — WRLES, Time-averaged WRLES, and RANS; - - - WMLES. LS: Lee Side; RC: Re-Circulation zone; SS: Stoss Side; C: Crest.

significantly in the streamwise direction: the Shields parameter is lowest on the lee side, where the flow velocity is directed upwards due to the recirculation and the bed-load transport rate is the lowest due to the prevailing downward flux of sediments due to gravity. Only on the stoss side, after re-attachment of the boundary layer, the shear stress increases to reach a maximum at the crest. Erosion prevails on deposition in this region: sediment is eroded from the stoss side of the dune, transported by the turbulent flow and then eventually deposited on the lee side (Marchioli et al., 2006).

Figure 12 shows the bed-load transport rate predicted by each model using WRLES, Time-averaged WRLES, WMLES, and RANS. For the Time-averaged WRLES, the bottom shear-stress calculated from the WRLES was then averaged in time on a moving window of $1.5\delta/u_\tau$. Despite the differences in magnitude, all the bed-load transport models behave qualitatively in a similar manner, except for the WMLES case, for which the estimated value of $\langle\Phi(\theta)\rangle_{zt}$ is significantly smaller. This reflects the inaccuracy of the wall model in the recirculating region, as explained in section 3.2. Note also that the RANS prediction is calculated by taking the time-average of the wall stress obtained from the WRLES. Thus, it is not affected by modelling errors. In an actual calculation, one would expect decreased accuracy in the non-equilibrium regions (e.g., reattachment, separation, or acceleration), and significant qualitative and quantitative differences

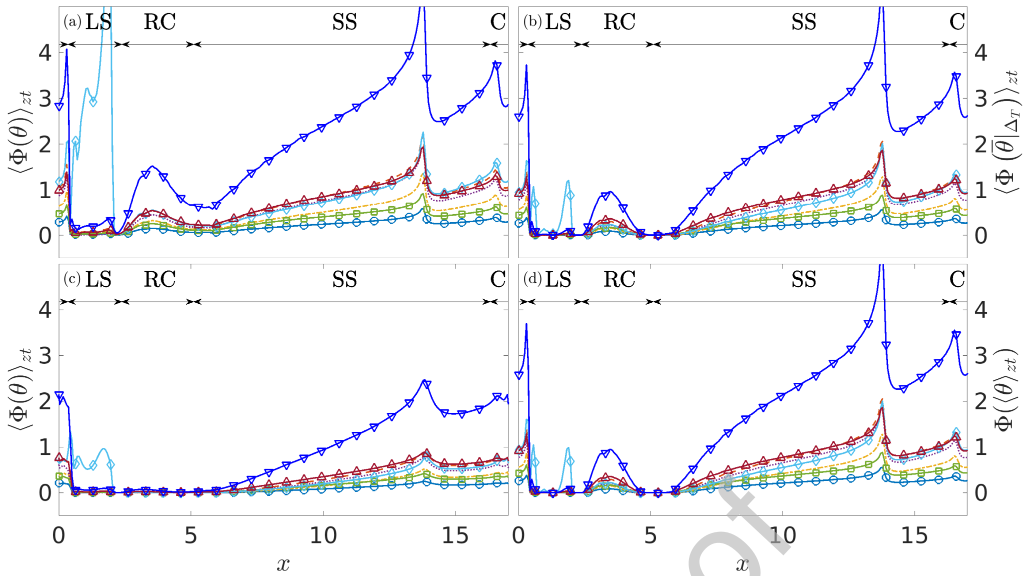

Figure 12: Comparison of the bed-load transport models at $d_* = 10$. WP06; EF76; P79; C02 FLvB76; vR84; N92; NG98. (a) WRLES; (b) Time-averaged WRLES over $1.5\delta/u_\tau$; (c) WMLES; (d) RANS. LS: Lee Side; RC: Re-Circulation zone; SS: Stoss Side; C: Crest.

between the RANS solution and the other methods. Short-time averaging decreases the level of the bottom shear-stress fluctuations, as observed in the plane channel. Thus, the WRLES produces results similar to the RANS simulation. We performed the same analysis also for the smaller and larger particles characterized by $d_* = 1$ and 50 (results not shown), and similar trends were obtained.

5. Conclusions

In this work we have examined how the space and time resolution used to compute the bottom shear-stress distribution affects the accuracy with which commonly-used bed-load transport models can predict the sediment transport rate in Euler-Euler simulations. To this aim, we have analyzed *a priori* three datasets from DNS of channel flow with smooth and rough walls, and from LES of the flow over a 2D dune.

We have shown that the high spatial and temporal resolution of the eddy-resolving Navier-Stokes solvers is incompatible with the RANS-based bed-load transport models for small values of the Shields parameter, $\langle\theta\rangle$. When $\langle\theta\rangle$ is below the critical value for incipient motion, the RANS approach predicts no bed-load transport, contrary to what experiments show; whereas the DNS and WRLES approaches overestimate the bed-load transport rate, and the WMLES approach yields the most accurate predictions. The discrepancies we observe, are limited to the range of the Shields parameter in which sediment transport is governed by bed-load transport (Chiodi et al., 2014). Within this range, therefore, an accurate evaluation of the bed-load transport is crucial for a correct prediction of bedforms formation and evolution. The bed-load predictions of the local model by Lee et al. (2012) show a qualitatively similar behaviour. However, the model is very accurate in the DNS case which provides the spatial and temporal resolution that the model was designed for.

The presence of roughness changes the near-wall flow characteristics, increasing the spatial and temporal variability of the flow field. The bed-load transport rate predicted in the rough-wall simulation follows the same trends, but shows greater discrepancies among DNS, WRLES, WMLES, and RANS for a wide range of $\langle\theta\rangle$, compared to the smooth-wall flow.

Short-time averaging of the local and instantaneous bottom shear-stress results in a decrease of its fluctuations, and, in turn, in a reduction of the occurrences in which it exceeds the critical Shields parameter. Short-time averaging on a window of the order the large-eddy turnover time, is found to improve the agreement of the bed-load transport rate predictions of DNS and WRLES in the smooth case. The rough channel flow case shows much larger near-wall velocity fluctuations and, therefore, requires a wider averaging window.

The flow over a two-dimensional dune was also simulated to investigate the effect of a change in the bed slope on the sediment transport rate. The bottom shear-stress is higher in the reattachment region and lower in the recirculation region, where the bed-load transport rate is strongly affected by the flow resolution (especially in WMLES and RANS). Although comparison with experimental data is still not possible, we found that short-time averaging leads to a prediction of the bed-load transport in WRLES that is closer to that predicted in RANS simulations. Errors in the calculation of the bottom shear-stress, however, affect the bed-load transport prediction significantly. Such errors would be present in WMLES that use the equilibrium-stress assumption, and perhaps in RANS solutions when the turbulence model encounters non-equilibrium regions.

Until now, most eddy-resolving calculations of sediment transport at Reynolds numbers representative of geophysical applications have been performed using WMLES and Eulerian sediment transport models. WMLES, for attached flows, exhibits a behaviour very similar to that of RANS solutions, and errors in the bed-load transport rates would be mainly due to the particular model chosen. If wall-resolved calculations were carried out, however, the wall-stress fluctuations could result in significant errors when the Shields parameter is close to its critical value. Only recently DNS-based calculations of bed-load transport that resolve the particles have become computationally feasible. The computational cost associated with the resolution required to represent the particle, however, limits this technique to fairly simple flow configurations at low Reynolds numbers (Vowinckel et al., 2019a), and cannot be extended, at present, to the range of flow parameters typically studied in WMLES calculations (Chou and Fringer, 2008; Khosronejad et al., 2011; Liu et al., 2019).

As the available computer power increases and eddy-resolving calculations become more popular, one should expect a transition from WMLES to WRLES. Our analysis shows that models dependent on the local and instantaneous flow field, such as the one designed by Lee et al. (2012) provide a suitably-accurate description of the bed-load transport when coupled with eddy-resolving techniques. Ancey (2020b) elegantly summarized the current situation on bed-load transport knowledge, strengths and limitations. One of the questions raised by this author was whether bed-load transport is driven by flow fluctuations; the analysis performed in this work suggests that, from a numerical perspective, the level of detail of the bed-load transport must be suitably tuned in order to improve model predictions and lead to better accordance with experimental measurements.

Acknowledgements

This research was supported by the Natural Science and Engineering Research Council of Canada (NSERC) under the Discovery Grant program (GDA), by the Canada Research Chair program (UP) and by the Ontario Trillium Scholarship (OTS) provided by the Government of Ontario. It was enabled in part by computational support provided by Compute Ontario (computeontario.ca) and Compute Canada (www.computecanada.ca). The authors would also like to thank the reviewers for the insightful comments received.

References

Ahadi, M., Bergstrom, D., Mazurek, K., 2018. Application of the Two-Fluid Model to Prediction of Sediment Transport in Turbulent Open Channel Flow. CFD .

Akiki, G., Balachandar, S., 2020. Shear-induced lift force on spheres in a viscous linear shear flow at finite volume fractions. Physics of Fluids 32. URL: https://doi.org/10.1063/5.0024642, doi:10.1063/5.0024642.

Ancey, C., 2020a. Bedload transport: a walk between randomness and determinism. Part 1. The state of the art. Journal of Hydraulic Research 58, 1–17. doi:10.1080/00221686.2019.1702594.

Ancey, C., 2020b. Bedload transport: a walk between randomness and determinism. Part 2. Challenges and prospects. Journal of Hydraulic Research 58, 18–33. doi:10.1080/00221686.2019.1702595.

Balachandar, R., Hyun, B., Patel, V., 2007. Effect of depth on flow over a fixed dune. Canadian Journal of Civil Engineering 34, 1587–1599. URL: http://www.nrcresearchpress.com/doi/10.1139/L07-068, doi:10.1139/L07-068.

Balachandar, S., 2009. A scaling analysis for point-particle approaches to turbulent multiphase flows. International Journal of Multiphase Flow 35, 801–810. URL: http://dx.doi.org/10.1016/j.ijmultiphaseflow.2009.02.013, doi:10.1016/j.ijmultiphaseflow.2009.02.013.

Balaras, E., 2004. Modeling complex boundaries using an external force field on fixed Cartesian grids in large-eddy simulations. Computers and Fluids 33, 375–404. doi:10.1016/S0045-7930(03)00058-6.

Batchelor, G.K., 1972. Sedimentation in a dilute dispersion of spheres. J. Fluid Mech. 52, 245–268. doi:10.1017/S0022112072001399.

Best, J., 1996. The Fluid Dynamics of Small-scale Alluvial Bedforms. Advances in Fluvial Dynamics and Stratigraphy , 67–125URL: https://ci.nii.ac.jp/naid/10007397378/en/.

Best, J., 2005. Kinematics, topology and significance of dune-related macroturbulence: some observations from the laboratory and field. Spec. Publ. 35 - Fluvial Sedimentology VII 35, 41–60. doi:10.1002/9781444304350.ch3.

Biegert, E., Vowinckel, B., Meiburg, E., 2017. A collision model for grain-resolving simulations of flows over dense, mobile, polydisperse granular sediment beds. Journal of Computational Physics 340, 105–127. URL: http://dx.doi.org/10.1016/j.jcp.2017.03.035, doi:10.1016/j.jcp.2017.03.035.

Bose, S., Park, G., 2018. Wall-Modeled Large-Eddy Simulation for Complex Turbulent Flows. Annual Review of Fluid Mechanics 50, 535–561. doi:10.1146/annurev-fluid-122316-045241.

Cao, Z., 1999. Equilibrium Near-Bed Concentration of Suspended Sediment. Journal of Hydraulic Engineering 125, 1270–1278.

Celik, I., Rodi, W., 1991. Suspended Sediment-Transport Capacity for Open Channel Flow. J. Hydraul. Eng. 117, 191–204.

Charru, F., Andreotti, B., Claudin, P., 2013. Sand ripples and dunes. Annual Review of Fluid Mechanics 45, 469–493. doi:10.1146/annurev-fluid-011212-140806.

Cheng, N., 2002. Exponential formula for bedload transport. Journal of Hydraulic Engineering 128, 942–946. doi:10.1061/(ASCE)0733-9429(2002)128:10(942).

Chiodi, F., Claudin, P., Andreotti, B., 2014. A two-phase flow model of sediment transport: Transition from bedload to suspended load. J. Fluid Mech. 755, 561–581. doi:10.1017/jfm.2014.422.

Chou, Y., Fringer, O., 2008. Modeling dilute sediment suspension using large-eddy simulation with a dynamic mixed model. Physics of Fluids 20, 1–14. doi:10.1063/1.3005863.

Chou, Y., Fringer, O., 2010. A model for the simulation of coupled flow-bed form evolution in turbulent flows. Journal of Geophysical Research: Oceans 115, 1–20. doi:10.1029/2010JC006103.

Coleman, S.E., Nikora, V.I., 2011. Fluvial dunes: Initiation, characterization, flow structure. Earth Surface Processes and Landforms 36, 39–57. doi:10.1002/esp.2096.

Davis, R., 1985. Sedimentation of nanoplastics. Ann. Rev. Fluid Mech. 17, 91–118.

Debnath, K., Chaudhuri, S., 2010a. Bridge Pier Scour in Clay-Sand Mixed Sediments at Near-Threshold Velocity for Sand. J. Hydraul. Eng. 136, 597–609. doi:10.1061/(asce)hy.1943-7900.0000221.

Debnath, K., Chaudhuri, S., 2010b. Cohesive sediment erosion threshold: A review. ISH Journal of Hydraulic Engineering 16, 36–56. doi:10.1080/09715010.2010.10514987.

Engelund, F., Fredsoe, J., 1976. A sediment transport model for straight alluvial channels. Nordic Hydrology 7, 293–306.

Fernandez Luque, R., van Beek, R., 1976. Erosion And Transport Of Bed-Load Sediment. Journal of Hydraulic Research 14, 127–144. doi:10.1080/00221687609499677.

Finn, J., Li, M., 2016. Regimes of sediment-turbulence interaction and guidelines for simulating the multiphase bottom boundary layer. International Journal of Multiphase Flow 85, 278–283. URL: http://dx.doi.org/10.1016/j.ijmultiphaseflow.2016.06.007, doi:10.1016/j.ijmultiphaseflow.2016.06.007.

Garcia, M., 1991. Entrainment of bed sediment into suspension. Journal of Hydraulic Engineering 117, 414–435.

Germano, M., Piomelli, U., Moin, P., Cabot, W.H., 1991. A dynamic subgrid-scale eddy viscosity model. Physics of Fluids A 3, 1760–1765. doi:10.1063/1.857955.

Guan, L., Salinas, J.S., Zgheib, N., Balachandar, S., 2021. The role of bed-penetrating Kelvin-Helmholtz vortices on local and instantaneous bedload sediment transport. Journal of Fluid Mechanics 911, 1–14. doi:10.1017/jfm.2020.1060.

Hantsis, Z., Piomelli, U., 2020. Roughness effects on scalar transport. Physical Review Fluids 5, 114607. URL: https://doi.org/10.1103/PhysRevFluids.5.114607, doi:10.1103/PhysRevFluids.5.114607.

Hay, A., Sheng, J., 1992. Determining suspended sand size and concentration from multifrequency acoustic backscatter. The Journal of the Acoustical Society of America 97, 15661–15677. URL: http://asa.scitation.org/doi/10.1121/1.407237, doi:10.1121/1.407237.

Jiménez, J., 2004. Turbulent flows over rough walls. Annual Review of Fluid Mechanics 36, 173–196. doi:10.1146/annurev.fluid.36.050802.122103.

Kawai, S., Larsson, J., 2012. Wall-modeling in large eddy simulation: Length scales, grid resolution, and accuracy. Physics of Fluids 24. doi:10.1063/1.3678331.

Keating, A., Piomelli, U., Bremhorst, K., Nešić, S., 2004. Large-eddy simulation of heat transfer downstream of a backward-facing step. Journal of Turbulence 5, 1–27. doi:10.1088/1468-5248/5/1/020.

Khosronejad, A., Kang, S., Borazjani, I., Sotiropoulos, F., 2011. Curvilinear immersed boundary method for simulating coupled flow and bed morphodynamic interactions due to sediment transport phenomena. Advances in Water Resources 34, 829–843. URL: http://dx.doi.org/10.1016/j.advwatres.2011.02.017, doi:10.1016/j.advwatres.2011.02.017.

Khosronejad, A., Sotiropoulos, F., 2014. Numerical simulation of sand waves in a turbulent open channel flow. J. Fluid Mech. 753, 150–216. doi:10.1017/jfm.2014.335.

Khosronejad, A., Sotiropoulos, F., 2017. On the genesis and evolution of barchan dunes: Morphodynamics. J. Fluid Mech. 815, 117–148. doi:10.1017/jfm.2016.880.

Kidanemariam, A., Uhlmann, M., 2014. Direct numerical simulation of pattern formation in subaqueous sediment. J. Fluid Mech. 750, 1–11. doi:10.1017/jfm.2014.284.

Kidanemariam, A., Uhlmann, M., 2017. Formation of sediment patterns in channel flow: minimal unstable systems and their temporal evolution. J. Fluid Mech. , 1–23.

Kim, J., Moin, P., 1985. Application of a Fractional-Step Method to Incompressible Navier-Stokes Equations. Journal of Computational Physics 59, 308–323.

Kocurek, G., R.C., E., D., M., 2010. How do bedform patterns arise? New views on the role of bedform interactions within a set of boundary conditions. Earth Surface Processes and Landforms 35, 51–63. doi:10.1002/esp.

Larsson, J., Kawai, S., Bodart, J., Bermejo-Moreno, I., 2016. Large eddy simulation with modeled wall-stress: recent progress and future directions. Mechanical Engineering Reviews 3. doi:10.1299/mer.15-00418.

Lau, Y., Engel, P., 1999. Inception of Sediment Transport on Steep Slopes. J. Hydraul. Eng. 125, 544–547.

Lee, H., Ha, M., Balachandar, S., 2012. Work-based criterion for particle motion and implication for turbulent bed-load transport. Physics of Fluids 24. doi:10.1063/1.4767541.

Lefebvre, A., 2019. Three-Dimensional Flow Above River Bedforms: Insights From Numerical Modeling of a Natural Dune Field (Río Paraná, Argentina). Journal of Geophysical Research: Earth Surface 124, 2241–2264. doi:10.1029/2018JF004928.

Lilly, D., 1992. A proposed modification of the Germano subgrid-scale closure method. Physics of Fluids A 4, 633–635. doi:10.1063/1.858280.

Liu, Y., Fang, H., Huang, L., He, G., 2019. Numerical simulation of the production of three-dimensional sediment dunes. Physics of Fluids 31, 096603–1. doi:10.1063/1.5108741.

Livingstone, I., Wiggs, G., Weaver, C., 2007. Geomorphology of desert sand dunes: A review of recent progress. Earth-Science Reviews doi:10.1016/j.earscirev.2006.09.004.

MacDonald, M., Hutchins, N., Chung, D., 2019. Roughness effects in turbulent forced convection. J. Fluid Mech. 861, 138–162. doi:10.1017/jfm.2018.900.

Marchioli, C., 2017. Large-eddy simulation of turbulent dispersed flows: a review of modelling approaches. Acta Mechanica 228, 741–771. doi:10.1007/s00707-017-1803-x.

Marchioli, C., Armenio, V., Salvetti, M., Soldati, A., 2006. Mechanisms for deposition and resuspension of heavy particles in turbulent flow over wavy interfaces. Physics of Fluids 18, 1–17. doi:10.1063/1.2166453.

Mazzuoli, M., Blondeaux, P., Vittori, G., Uhlmann, M., Simeonov, J., Calantoni, J., 2020. Interface-resolved direct numerical simulations of sediment transport in a turbulent oscillatory boundary layer. J. Fluid Mech. 885, 1–33. doi:10.1017/jfm.2019.1012.

Meiburg, E., Kneller, B., 2010. Turbidity currents and their deposits. Annu. Rev. Fluid Mech. 42, 135–156. doi:10.1146/annurev-fluid-121108-145618.

Meneveau, C., Lund, T., Cabot, W., 1996. A Lagrangian dynamic subgrid-scale model of turbulence. J. Fluid Mech. 319, 353–385. doi:10.1017/S0022112096007379.

Meyer-Peter, E., Müller, R., 1948. Formulas for Bed-Load Transport. Proceedings of the 2nd Meeting of the International Association of Hydraulic Research , 39–64doi:1948-06-07.

Nielsen, P., 1992. Coastal bottom boundary layers and sediment transport. 1 ed., World Scientific Publishing, Singapore.

Niño, Y., García, M., 1998. Using Lagrangian particle saltation observations for bedload sediment transport modelling. Hydrol. Process. 12, 1197–1218. doi:10.1002/(SICI)1099-1085(19980630)12:8<1197::AID-HYP612>3.0.CO;2-U.

Niño, Y., Lopez, F., García, M., 2003. Threshold for particule entrainement into suspension. Sedimentology 50, 247–263. doi:10.1046/j.1365-3091.2003.00551.x.

Oliver, D., 1961. The sedimentation of suspensions of closely-sized spherical particles. Technical Report. University of Birmingham.

Omidyeganeh, M., Piomelli, U., 2011. Large-eddy simulation of two-dimensional dunes in a steady, unidirectional flow. Journal of Turbulence 12, 1–31. doi:10.1080/14685248.2011.609820.

Paintal, A.S., 1971. La notion de tendion de frottement critique dans les cours dâĂŹeau àlit mobile. Journal of Hydraulic Research 9, 91–113. doi:10.1080/00221687109500339.

Paola, C., Voller, V.R., 2005. A generalized Exner equation for sediment mass balance. Journal of Geophysical Research: Earth Surface 110, 1–8. doi:10.1029/2004JF000274.

Papadopoulos, K., Nikora, V., Vowinckel, B., Cameron, S., Jain, R., Stewart, M., Gibbins, C., Fröhlich, J., 2020. Double-averaged kinetic energy budgets in flows over mobile granular beds: insights from DNS data analysis. Journal of Hydraulic Research 58, 653–672. doi:10.1080/00221686.2019.1661291.

Parker, G., 1979. Hydraulic geometry of active gravel rivers. Journal of the Hydraulics Division, ASCE 105, 1185–1201.

Parsons, D., Walker, I., Wiggs, G., 2004. Numerical modelling of flow structures over idealized transverse aeolian dunes of varying geometry. Geomorphology 59, 149–164. doi:10.1016/j.geomorph.2003.09.012.

Parsons, D.R., Best, J.L., Orfeo, O., Hardy, R.J., Kostaschuk, R., Lane, S.N., 2005. Morphology and flow fields of three-dimensional dunes, Rio Paraná, Argentina: Results from simultaneous multibeam echo sounding and acoustic Doppler current profiling. Journal of Geophysical Research: Earth Surface 110, 1–9. doi:10.1029/2004JF000231.

Piomelli, U., 2008. Wall-layer models for large-eddy simulations. Progress in Aerospace Sciences 44, 437–446. doi:10.1016/j.paerosci.2008.06.001.

Reesink, A., Bridge, J.S., 2009. Influence of bedform superimposition and flow unsteadiness on the formation of cross strata in dunes and unit bars - Part 2, further experiments. Sedimentary Geology 222, 274–300. URL: http://dx.doi.org/10.1016/j.sedgeo.2009.09.014, doi:10.1016/j.sedgeo.2009.09.014.

Reesink, A., Parsons, D., Ashworth, P., Best, J., Hardy, R., Murphy, B., McLelland, S., Unsworth, C., 2018. The adaptation of dunes to changes in river flow. Earth-Science Reviews 185, 1065–1087. doi:10.1016/j.earscirev.2018.09.002.

Reesink, A.J., Bridge, J.S., 2007. Influence of superimposed bedforms and flow unsteadiness on formation of cross strata in dunes and unit bars. Sedimentary Geology 202, 281–296. doi:10.1016/j.sedgeo.2007.02.005.

van Rijn, L., 1984a. Sediment Transport, Part II: Suspended Load Transport. J. Hydraul. Eng. 110, 1613–1641.

van Rijn, L., 1984b. Sediment Transport, Part III: Bed Forms and Alluvial Roughness. J. Hydraul. Eng. 110, 1733–1754.

van Rijn, L., 1987. Mathematical modelling of morphological processes in the case of suspended sediment transport. Ph.D.

thesis. Delft University of Technology.

van Rijn, L., 1993. Principles of Sediment Transport in Rivers, Estuaries and Coastal Seas. 1 ed., Publications, Aqua, Amsterdam.

van Rijn, L.C., 1984c. Sediment Transport , Part I: Bed Load Transport. J. Hydraul. Eng. 110, 1431–1456. doi:10.1016/j.optcom.2012.06.066.

Salim, S., Pattiaratchi, C., 2020. Sediment resuspension due to near-bed turbulent coherent structures in the nearshore. Continental Shelf Research 194, 1–15. URL: https://doi.org/10.1016/j.csr.2020.104048, doi:10.1016/j.csr.2020.104048.

Scalo, C., Piomelli, U., Boegman, L., 2012. High-Schmidt-number mass transport mechanisms from a turbulent flow to absorbing sediments. Physics of Fluids 24. doi:10.1063/1.4739064.

Scherer, M., Kidanemariam, A., Uhlmann, M., 2020. On the scaling of the instability of a flat sediment bed with respect to ripple-like patterns. J. Fluid Mech. 900, 1–29.

Scotti, A., 2006. Direct numerical simulation of turbulent channel flows with boundary roughened with virtual sandpaper. Physics of Fluids 18. doi:10.1063/1.2183806.

Shields, A., 1936. Anwendung der Aehnlichkeitsmechanik und der Turbulenzforschung auf die Geschiebebewegung. Ph.D. thesis. Technical University Berlin.

Spalart, P., 1986. Numerical study of sink-flow boundary layers. J. Fluid Mech. 172, 307–328. doi:10.1017/S0022112086001751.

Stoesser, T., Braun, C., García-Villalba, M., Rodi, W., 2008. Turbulence Structures in Flow over Two-Dimensional Dunes. Journal of Hydraulic Engineering 134, 42–55. doi:10.1061/(ASCE)0733-9429(2008)134:1(42).

Unsworth, C., Parsons, D., Hardy, R., Reesink, A., Best, J., Ashworth, P., Keevil, G., 2018. The Impact of Nonequilibrium Flow on the Structure of Turbulence Over River Dunes. Water Resources Research 54, 6566–6584. doi:10.1029/2017WR021377.

Venditti, J., Church, M., Bennett, S., 2005. On the transition between 2D and 3D dunes. Sedimentology 52, 1343–1359. doi:10.1111/j.1365-3091.2005.00748.x.

Vittori, G., Blondeaux, P., Mazzuoli, M., Simeonov, J., 2020. Sediment transport under oscillatory flows. International Journal of Multiphase Flow , 1–25.

Vowinckel, B., 2021. Incorporating grain-scale processes in macroscopic sediment. Acta Mechanica URL: https://doi.org/10.1007/s00707-021-02951-4, doi:10.1007/s00707-021-02951-4.

Vowinckel, B., Biegert, E., Luzzatto-Fegiz, P., Meiburg, E., 2019a. Consolidation of freshly deposited cohesive and non-cohesive sediment: Particle-resolved simulations. Physical Review Fluids 4, 1–20. doi:10.1103/PhysRevFluids.4.074305.

Vowinckel, B., Jain, R., Kempe, T., Fröhlich, J., 2016. Entrainment of single particles in a turbulent open-channel flow : a numerical study. Journal of Hydraulic Research doi:10.1080/00221686.2016.1140683.

Vowinckel, B., Nikora, V., Kempe, T., Fröhlich, J., 2017a. Momentum balance in flows over mobile granular beds: application of double-averaging methodology to DNS data. Journal of Hydraulic Research 55, 190–207. doi:10.1080/00221686.2016.1260656.

Vowinckel, B., Nikora, V., Kempe, T., Fröhlich, J., 2017b. Spatially-averaged momentum fluxes and stresses in flows over mobile granular beds: a DNS-based study. Journal of Hydraulic Research 55, 208–223. doi:10.1080/00221686.2016.1260658.

Vowinckel, B., Withers, J., Luzzatto-Fegiz, P., Meiburg, E., 2019b. Settling of cohesive sediment: particle-resolved simulations. J. Fluid Mech. 858, 5–44. URL: http://arxiv.org/abs/1804.05943, doi:10.1017/jfm.2018.757.

Warren, A., 2013. Dunes: Dynamics, Morphology, History. Wiley-Blackwell. doi:10.1002/9781118295786.

Weaver, C., Wiggs, G., 2011. Field measurements of mean and turbulent airflow over a barchan sand dune. Geomorphology 128, 32–41. URL: http://dx.doi.org/10.1016/j.geomorph.2010.12.020, doi:10.1016/j.geomorph.2010.12.020.

Wong, M., Parker, G., 2006. Reanalysis and correction of bed-load relation of Meyer-Peter and Mü;ller using their own database. Journal of Hydraulic Engineering 132, 1159–1168. doi:10.1061/(ASCE)0733-9429(2006)132:11(1159).

Wu, F., Chou, Y., 2003. Rolling and lifting probabilities for sediment entrainment. Journal of Hydraulic Engineering 129, 110–119. doi:10.1061/(ASCE)0733-9429(2003)129:2(110).

Wu, W., Piomelli, U., Yuan, J., 2019. Turbulence statistics in rotating channel flows with rough walls. International Journal of Heat and Fluid Flow 80. URL: https://doi.org/10.1016/j.ijheatfluidflow.2019.108467, doi:10.1016/j.ijheatfluidflow.2019.108467.

Wu, W., Soligo, G., Marchioli, C., Soldati, A., Piomelli, U., 2017. Particle resuspension by a periodically forced impinging jet. J. Fluid Mech. 820, 284–311. doi:10.1017/jfm.2017.210.

Yamaguchi, S., Giri, S., Shimizu, Y., Nelson, J., 2019. Morphological Computation of Dune Evolution with Equilibrium and Non-Equilibrium Sediment-Transport Models. Water Resources Research 55, 8463–8477. doi:10.1029/2018WR024166.

Yuan, J., Piomelli, U., 2014. Roughness effects on the Reynolds stress budgets in near-wall turbulence. J. Fluid Mech. 760. doi:10.1017/jfm.2014.608.

Zedler, E., Street, R., 2001. Large-Eddy Simulation of Sediment Transport: Currents over Ripples. Journal of Hydraulic Engineering 127, 444–452.

Zedler, E., Street, R., 2006. Sediment transport over ripples in oscillatory flow. Journal of Hydraulic Engineering 132, 180–193. doi:10.1061/(asce)0733-9429(2006)132:2(180).

Zgheib, N., Fedele, J.J., Hoyal, D.C., Perillo, M.M., Balachandar, S., 2018a. Direct Numerical Simulation of Transverse Ripples: 1. Pattern Initiation and Bedform Interactions. Journal of Geophysical Research: Earth Surface 123, 448–477. doi:10.1002/2017JF004398.

Zgheib, N., Fedele, J.J., Hoyal, D.C., Perillo, M.M., Balachandar, S., 2018b. Direct Numerical Simulation of Transverse Ripples: 2. Self-Similarity, Bedform Coarsening, and Effect of Neighboring Structures. Journal of Geophysical Research: Earth Surface 123, 478–500. doi:10.1002/2017JF004399.

Declaration of interests 1754

☒ The authors declare that they have no known competing financial interests or personal relationships that could have appeared to influence the work reported in this paper.

☐The authors declare the following financial interests/personal relationships which may be considered as potential competing interests: